J. Fluid Mech. (2007), *vol.* 574, *pp.* 25–58. © 2007 Cambridge University Press
doi:10.1017/S0022112006003995 Printed in the United Kingdom

Numerical simulation of active separation control by a synthetic jet

JULIEN DANDOIS[1], ERIC GARNIER[1] AND PIERRE SAGAUT[2,3]

[1]ONERA, Applied Aerodynamic Department, BP 72, 29 av. de la division Leclerc, 92322 Châtillon Cedex, France

[2]Laboratoire de Modélisation en Mécanique, Université Pierre et Marie Curie – Paris 6, Boite 162, 4 Place Jussieu 75252, Paris cedex 5, France

[3]ONERA, CFD and Aeroacoustics Department, 92322 Châtilon Cedex, France

(Received 2 May 2006 and in revised form 28 August 2006)

Direct numerical simulation (DNS) and large-eddy simulation (LES) are carried out to investigate the frequency effect of zero-net-mass-flux forcing (synthetic jet) on a generic separated flow. The selected test case is a rounded ramp at a Reynolds number based on the step height of 28 275. The incoming boundary layer is fully turbulent with $R_\theta = 1410$. The whole flow in the synthetic jet cavity is computed to ensure an accurate description of the actuator effect on the flow field. In a first step, DNS is used to validate LES of this particular flow. In a second step, the effect of a synthetic jet at two reduced frequencies of 0.5 and 4 (based on the separation length of the uncontrolled case and the free-stream velocity) is investigated using LES. It is demonstrated that, with a proper choice of the oscillating frequency, separation can be drastically reduced for a velocity ratio between the jet and the flow lower than one. The low frequency is close to the natural vortex shedding frequency. Two different modes of the synthetic jet have been identified. A *vorticity-dominated mode* is observed in the low-frequency forcing case for which the separation length is reduced by 54 %, while an *acoustic-dominated mode* is identified in the high-frequency forcing case for which the separation length is increased by 43 %. The decrease of the separation length in the low-frequency forcing case is correlated with an increase of the turbulent kinetic energy level and consequently with an increase of the entrainment in the separated zone. A linear inviscid stability analysis shows that the increase of the separation length in the high-frequency forcing case is due to a modification of the mean velocity profile suggested by Stanek and coworkers. The result is a lower amplification of the perturbations and consequently, a lower entrainment into the mixing layer. To our knowledge, it is the first time that Stanek's hypothesis has been assessed, thanks to numerical simulations of fully turbulent flow.

1. Introduction

Separated flows occur in a wide range of engineering applications such as airfoils at high angle of attack, turbomachines, combustors, diffusers, etc. Separation generally has a negative impact on performance because it leads to reduced lift, increased drag and pressure loss, noise generation and structural loads, etc.

Recently, in order to improve aerodynamic performance, many attempts have been made to control turbulent separated flows. Among the available actuators for flow

https://doi.org/10.1017/S0022112006003995 Published online by Cambridge University Press

control, synthetic jets seem promising since they have been proven to efficiently control separation (Seifert *et al.* 1993), to enhance mixing (Chen *et al.* 1999) and to enable vector thrust (Smith & Glezer 2002). The main advantage of synthetic jets compared to steady blowing or suction devices is that they require one or two orders of magnitude less momentum to produce equivalent effects (Seifert *et al.* 1993). They also do not require a complex piping system since the momentum expulsion is only due to the periodic motion of a diaphragm or a piston on the lower wall of a cavity.

Many studies have been devoted to separated flows in the past few decades. Among them, the flow over a backward-facing step has received a considerable attention because of its simple geometry and the fact that separation point is fixed. Table 1 presents a review of the values of the main flow frequencies reported in the literature for several generic separated flows: flow over backward-facing steps, the recirculation bubble at the leading edge of blunt flat plates and fence flows.

Two instabilities are generally observed in the separated region past a backward-facing step: a convective one and an absolute one (see Huerre & Rossi 1998 for the convective/absolute instability definition). The convective instability is the Kelvin–Helmholtz (K-H) instability which originates in the natural periodic roll-up of the shear layer, and leads to the growth of spanwise structures. This instability has a Strouhal number based on the momentum thickness of the boundary layer at the separation point θ of $St_\theta = 0.012$. As indicated by Hasan (1992), the natural instability frequency for the shear layer scales neither with the ramp height nor with the separation length but rather with a shear layer characteristic length scale such as the momentum or the vorticity thickness. The shear layer instability reduces to the shedding mode via one or more vortex merging processes (Hasan 1992). To obtain a relevant frequency scaling of the shedding mode, we define a Strouhal number F^+ based on the separation length L and the free-stream velocity U_∞. As it can be seen in table 1, the shedding mode has a characteristic reduced frequency F^+ which ranges from 0.6 to 0.8. Sigurdson (1995) proposed a different scaling based on the separation bubble height H and the velocity at the separation point U_s, which correlates the shedding frequencies of a wide variety of separated flows. This scaling yields values near 0.07–0.09 for all geometries. But a notable drawback is that it requires knowledge of the separation bubble height which is often not measured in the experiments. For backward-facing step flows, $L/H = 7$ and $U_s = U_\infty$ is used in Sigurdson (1995) to convert the F^+ scaling into frequency scaling. The absolute instability is also called the low-frequency flapping mode of the shear layer and it has been attributed by Eaton & Johnston (1980) to an instantaneous imbalance between entrainment of fluid by the mixing layer from the recirculation region and injection of fluid inside the separation bubble near the reattachment point. The characteristic frequency of this phenomenon is, depending on the authors, 5 to 12 times lower than the shedding mode frequency, leading to $0.12 < F^+ < 0.18$. It should be mentioned that there are different opinions about the definition and physical explanation of the shedding and flapping phenomena.

The efficiency of the shear layer forcing is observed to strongly depend on the forcing frequency. For example, forcing at the natural shear layer instability frequency inhibits merging and regulates the spacing between vortices (Ho & Huang 2002). On the other hand, forcing at a subharmonic frequency of the natural instability enhances vortex merging and the growth rate of the shear layer.

Active separation control over ramps or backward-facing steps has been studied experimentally and numerically by many authors. Bhattacharjee, Scheelke & Troutt

https://doi.org/10.1017/S0022112006003995 Published online by Cambridge University Press

https://doi.org/10.1017/S0022112006003995 Published online by Cambridge University Press

Author	Configuration type	Study type	h (mm)	Re_h	L/h	Kelvin–Helmholtz frequency, St_θ	Shedding frequency, F^+	Flapping frequency, F^+
Mabey (1972)	review	E					0.6	
Eaton & Johnston (1980)	BFS	E	50.8	$Re_\theta = 240$	7	$St_\theta = 0.015$	0.52	
				$Re_\theta = 850$	7.95		0.52	
Driver, Seegmiller & Marvin (1983)	BFS	E	12.7	40000	6.1		0.7 . . . 0.8	
Cherry, Hillier & Latour (1984)	FP	E	$D = 38.1$	32000	$x_r/D = 4.8$		0.7	<0.125
Troutt, Sheelke & Norman (1984)	BFS	E	56	45000	6		1.5 . . . 3.9	
Kiya & Sasaki (1985)	FP	E	$2H = 20$	26000	10.1		0.6	0.12
Adams & Johnston (1988*a*)	BFS	E	38.1	800 . . . 40000	4.9 . . . 6.7		0.49	0.16
Simpson (1989)	review	E					0.6 . . . 0.8	<0.1
Devenport & Sutton (1991)	BFS	E	35	35000	1.47		0.74	0.18
Neto *et al.* (1993)	BFS	N		38000	8.1		0.65	
Sigurdson (1995)	CC	E	$D = 165$	42000 . . . 132000	7		0.49 ($f.h/U_s = 0.07$)	
Chun & Sung (1996)	BFS	E	50	13000 . . . 33000	6.75 . . . 7.8	$St_\theta = 0.012$	1	
Le, Moin & Kim (1997)	BFS	N	ER = 1.2	5000	6.28		0.41	
Huang & Fiedler (1997)	BFS	E	20	4300	5		0.2	
Heenan & Morrison (1998)	BFS	E	75	190000	5.5		1	0.1
Yang & Voke (2001)	FP	E		$Re_d = 3450$	$x_r/d = 2.6$		0.77	0.12 . . . 0.3
Tihon, Legrand & Legentilhomme (2001)	BFS	E	20	4800	5.1		0.65	0.15
Spazzini *et al.* (2001)	BFS	E	22	3500 . . . 16000	5 . . . 6.5		1	0.08
Lee & Sung (2002)	BFS	E	50	33000	7.4		0.48	0.1
Naguib & Hudy (2003) and Hudy, Naguib & Humphreys (2003)	F	E	$2H = 35$	$Re_{2H} = 25600$	7.8		0.6 . . . 0.9	0.12 . . . 0.18

TABLE 1. Kelvin–Helmholtz, shedding and flapping frequencies for different flows (configuration type: BFS = backward-facing step, FP = flat-plate leading edge, CC = circular cylinder aligned coaxially with the free stream F = fence; study type: E = Experiment study, N = Numerical study).

(1986), Chun & Sung (1996), Yoshioka, Obi & Masuda (2001*a*, *b*) Wengle *et al.* (2001) and Dejoan & Leschziner (2004), have reported a reduction of the recirculation length by about 30 % for an optimal Strouhal number $St_h \simeq 0.2$. This frequency does not correspond to the low-frequency flapping of the shear layer but rather to the mixing layer shedding mode at $St_\theta = 0.012$ (Chun & Sung 1996). Chun & Sung (1998) have found a higher optimal forcing Strouhal number $St_\theta = 0.025$ and attribute this discrepancy to their low Reynolds number. Liu, Kang & Sung (2005) have also found a slightly higher optimal Strouhal number $St_h \simeq 0.275$. Neumann & Wengle (2004*b*) have performed a large-eddy simulation of separation control over a rounded step. They also found an optimal Strouhal number $St_h \simeq 0.2$ but this frequency does not correspond to the optimal frequency $St_\theta = 0.012$ of sharp-edge backward-facing step flows. For a hump model, Seifert & Pack (2002) report an optimal reduced frequency equal to $F^+ = 1.6$. For their inclined surface, Darabi & Wygnanski (2004*a*, *b*) have reported an optimal excitation frequency $F^+ = 1.5$ for minimizing the reattachment time.

Besides control at reduced frequency $F^+ = O(1)$, a second control strategy based on a high-frequency actuation ($F^+ = O(10)$) has been suggested recently. Amitay & Glezer (2002) and Glezer, Amitay & Honohan (2005) observed that high-frequency forcing is able to increase lift and reduce drag on an airfoil without the drawback of increasing lift fluctuations as in the case of low-frequency forcing. The reason is a virtual modification of the airfoil shape by the formation of a small recirculation zone close to the actuator location which changes the pressure distribution. Using the same kind of forcing, Stanek *et al.* (2000) observed a drastic reduction of the noise level in their experiment on flow over a cavity. In particular, a strong attenuation of the large-scale fluctuations has been found in the pressure spectra. Stanek *et al.* (2002*a*, *b*), Vukasinovic, Lucas & Glezer (2005) and Rusak & Eisele (2005) explain this observation as a modification of the mean velocity profile which stabilizes the mean flow and prevents the growth of the Kelvin–Helmholtz instability.

Being aware of the importance of the excitation frequency, the main aim of the present paper is to investigate the effect of two different flow control strategies: low-frequency forcing and high-frequency forcing. Additionally, a secondary objective is to demonstrate numerically that separation can be drastically reduced on a smooth ramp by means of a synthetic jet with an exhaust velocity lower than the free-stream one. This point is of particular importance for practical purposes since available synthetic jet actuators have limited exhaust velocities.

Furthermore, accurate prediction of the mean separation point over smooth ramps is still a challenging issue because separation is governed by an adverse pressure gradient, unlike backward-facing step flows in which it is fixed by the geometry. With accuracy reasons, advanced numerical methods such as direct numerical simulations (DNS) and large-eddy simulation (LES) are used. With the same goal of accuracy, the flow in the whole synthetic jet cavity is computed.

The article is organized as follows. In § 2, the flow configuration is presented. The key elements of the numerical method, subgrid modelling, computational grid and boundary conditions are described in § 3. In § 4, LES of the uncontrolled case is validated via comparison with DNS results. The separated region features are compared to those of free mixing layers and backward-facing step flows. Natural instability frequencies of this flow are found. In § 5, the influence of the synthetic jet frequency on the separation bubble is studied by means of LES in order to limit the computational cost. Lastly, the main results are summarized in § 6.

https://doi.org/10.1017/S0022112006003995 Published online by Cambridge University Press

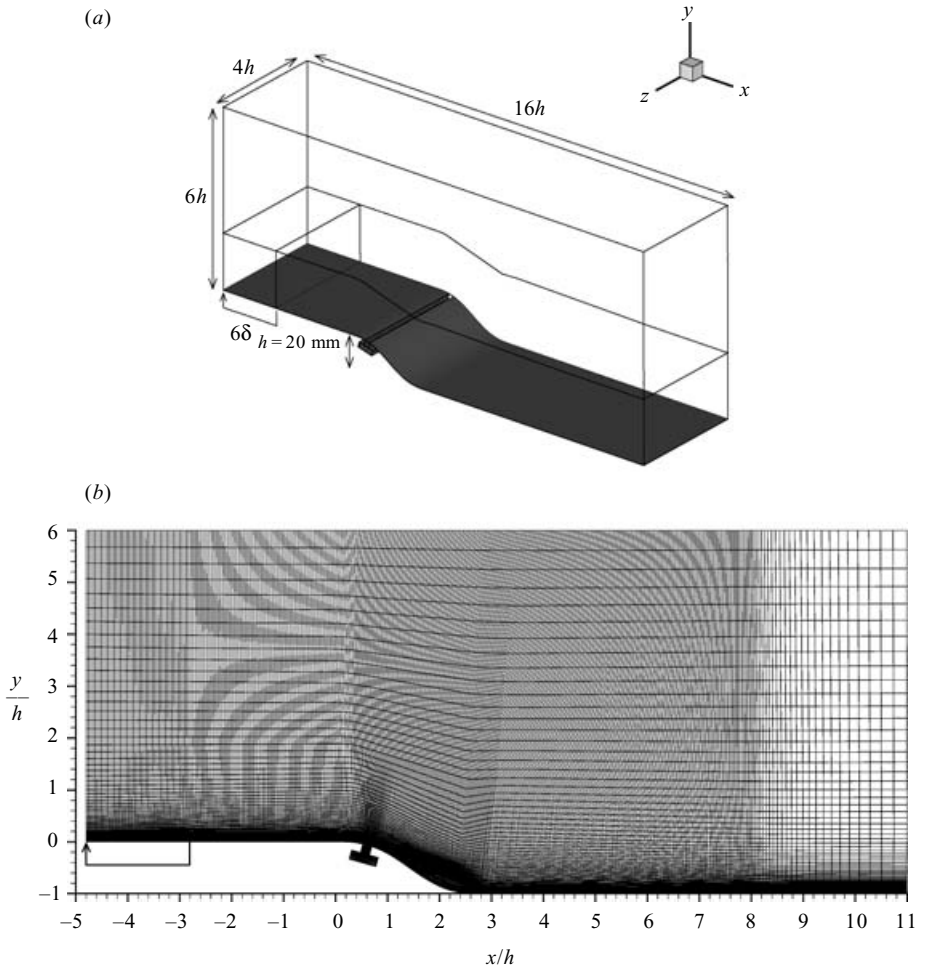


FIGURE 1. (*a*) Flow configuration with the synthetic jet cavity and the computational domain dimensions and (*b*) LES grid in the (x, y)-plane.

2. Flow configuration

The flow configuration is displayed in figure 1(*a*). We consider a rounded backward-facing step with shape is defined by

$$\frac{y}{h} = \frac{1}{2\pi}\left(\sin\left(\frac{a\pi x}{h}\right) - \frac{a\pi x}{h}\right), \quad \frac{x}{h} \in \left[0, \frac{2}{a}\right] \tag{2.1}$$

with $a = 0.703$. The step height is $h = 20$ mm and the maximum slope is equal to 35°. This configuration is selected because of its relevance for separated flows encountered in aeronautical applications such as air intakes. However, in order to prevent some difficulties related to internal flow simulations, an external flow is considered here. The stagnation pressure is 20 011 Pa and the stagnation temperature is 283 K. The kinematic viscosity ν is equal to $7.15 \times 10^{-5}\,\mathrm{m^2\,s^{-1}}$. The Mach number is set equal to 0.3 and the free-stream velocity is $101\,\mathrm{m\,s^{-1}}$. The boundary layer thickness δ at the inlet plane of the computational domains is $0.5h$ and its momentum thickness θ

https://doi.org/10.1017/S0022112006003995 Published online by Cambridge University Press

is $0.05h$. The Reynolds number based on the momentum thickness is $R_\theta = 1410$ as in the DNS of a turbulent boundary layer of Spalart (1988). The Reynolds number based on the step height and the free-stream velocity Re_h is 28 275. The synthetic jet orifice consists of a two-dimensionnal slot of width $d = \delta/3 = h/6$. Its windward edge is located at the mean separation point of the uncontrolled flow computed by DNS following the methodology proposed in Neumann & Wengle (2004*b*). The cavity height is d and its width is $3d$.

The coordinate system is the following: x is oriented in the streamwise direction, y is vertical and z is in the spanwise direction. The origin is located at the beginning of the ramp.

3. Numerical method

The code FLU3M is a finite-volume solver for the compressible Navier–Stokes equations. For LES, the filtered equations are obtained using the formalism developed by Vreman (1995). The subgrid-scale model is the selective mixed scale model detailed by Sagaut (2002). The time integration is carried out by means of the second-order-accurate backward scheme of Gear. More details about the numerical method are available in Péchier, Guillen & Gayzac (2001). The time step is taken equal to 0.0025 h/U_∞ for all simulations. The spatial scheme is the one proposed by Mary & Sagaut (2002). It is based on a modification of the AUSM+(P) scheme (see Edwards & Liou 1998) whose dissipation is proportional to the local fluid velocity, and so it is well adapted to low-Mach-number simulations. The accuracy of the solver for DNS and LES purposes has been assessed in various applications (Mary & Sagaut 2002; Larchevêque *et al.* 2004; Deck 2005*a*, *b*; Dandois, Garnier & Sagaut 2006).

Two grids with the same spatial extent are used for the computations. Each is composed of a three-dimensional grid which encompasses the turbulent region and a two-dimensional region for $y/h > 2$ in which the flow is quasi-potential. The streamwise length of the computational domain is $16h$ ($5.5h$ upstream of the separation point and $7.5h$ downstream of the reattachment point), its spanwise extent is $4h$ and its height is $6h$ upstream of the ramp. The DNS grid includes $1008 \times 68 \times 400 = 28 \times 10^6$ cells. Grid spacings are $\Delta x^+ = 16$, $\Delta y^+_{min} = 0.5$ and $\Delta z^+ = 12$, in agreement with the grid resolutions reported in the literature of DNS of separated flows: $\Delta x^+ = 10$, $\Delta y^+_{min} = 0.3$ and $\Delta z^+ = 15$ in Le *et al.* (1997) and $\Delta x^+ = 18.3$, $\Delta y^+_{min} = 0.11$ and $\Delta z^+ = 10.5$ in Na & Moin (1998). The wall unit scaling is based on the friction velocity taken at the inlet of the computational domain. The LES grid has $345 \times 68 \times 268 = 7 \times 10^6$ cells. Grid spacings are: $\Delta x^+ = 50$, $\Delta y^+_{min} = 0.5$ and $\Delta z^+ = 18$. A view of the LES grid in the (x, y)-plane is displayed in figure 1(*b*).

Computations have been performed on four NEC-SX6 processors. The CPU time required for one flow-through time (i.e. the time it takes for a fluid particle in the free stream to cross the computational domain) is 144 hours for the DNS and 36 hours for the LES. In the uncontrolled case, samples were collected during fifteen and twenty five flow-through times for the DNS and the LES respectively. In the controlled cases, a transient time equivalent to two flow-through times was necessary to reach the periodic regime. Then, five flow-through times were found sufficient to obtain converged statistics.

To simulate the diaphragm displacement, a blowing/suction condition with a top-hat distribution with sinusoidal time variation is implemented on the whole cavity bottom surface: $u(x, t) = U_0 \cos(2\pi f t)$. This boundary condition has been successfully validated in a previous study (Dandois *et al.* 2006) and by comparison with

https://doi.org/10.1017/S0022112006003995 Published online by Cambridge University Press

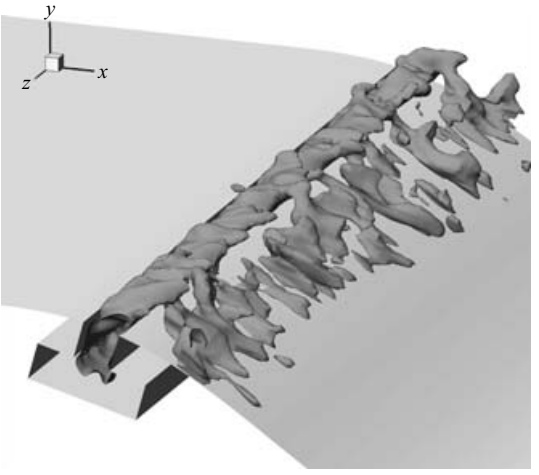


FIGURE 2. Vertical velocity isosurface $v/U_\infty = 0.2$.

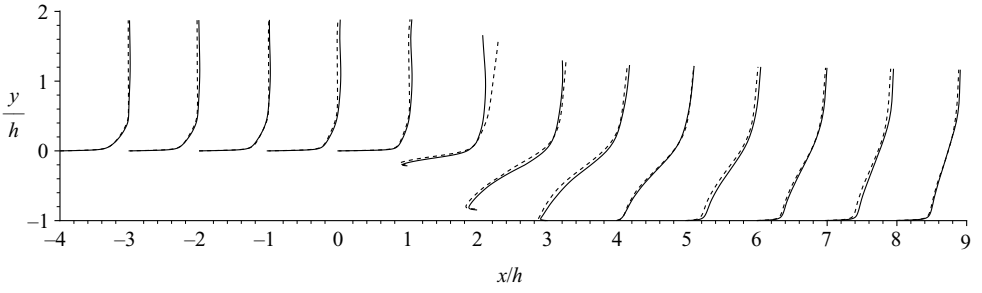


FIGURE 3. Time-averaged streamwise velocity $x/h + u/U_\infty$ (solid line: DNS, dashed line: LES).

simulations based on the arbitrary Lagrangian Eulerian (ALE) numerical technique for which the real sinusoidal motion of the bottom surface was computed. Figure 2 displays a vertical velocity isosurface during the blowing phase. It emphasizes the three-dimensional character of the flow in the cavity, showing that the computation of the whole actuator cavity is a mandatory requirement to recover an accurate description of the synthetic jet effect on the separation.

For these computations, a realistic turbulent inflow boundary condition based on an extraction/rescaling technique is used. The technique used in the present work is the extension to compressible flows of the method proposed in Lund, Wu & Squires (1998) given in Sagaut *et al.* (2004).

4. LES validation and analysis

4.1. *Global analysis*

The DNS computation is used here as a database to validate the LES results. Figure 3 displays the evolution of the mean streamwise velocity u. Both computations lead to very similar results. Only slight differences occur in the recirculation zone, but are lower than 6 %. It can be noted that the same maximum backflow velocity $-0.16U_\infty$ is found in both computations.

https://doi.org/10.1017/S0022112006003995 Published online by Cambridge University Press

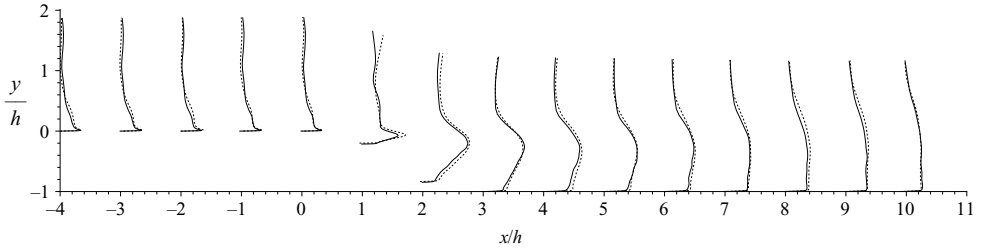


FIGURE 4. Time-averaged streamwise velocity fluctuation $x/h + u_{rms}/40$ (solid line: DNS, dashed line: LES).

The time-averaged streamwise positions of the separation x_s and reattachment x_r points are $x_s/h = 0.53$ (0.51) and $x_r/h = 3.93$ (3.96) for the DNS and the LES, respectively. Compared to the DNS, the LES separation length $(x_r - x_s)/h$ is overestimated by only 1.6 %. A Reynolds-averaged simulation based on the Spalart–Allmaras turbulence model and the rotation correction by Dacles-Mariani *et al.* (1995) yields $x_s/h = 0.55$ and $x_r/h = 6.3$. The separation point is predicted well but the reattachment is too far downstream which leads to an overestimation of the separation bubble extent by about 70 %.

The streamwise velocity fluctuation u_{rms} (see figure 4) obtained by LES is in very good agreement with the DNS, in particular in the separated region.

A comparison of the instantaneous turbulent structures for the two cases is displayed in figure 5. Because of the turbulent incoming boundary layer, two-dimensional spanwise structures are not visible with a Q-criterion isosurface plot but they could be observed with pressure isosurfaces or by using the first POD modes as in Neumann & Wengle (2004*a*). As expected, figure 5 shows finer turbulent structures in the DNS solution than in the LES field.

4.2. *Mixing layer and separation bubble analysis*

This section is devoted to the description of the transition region between the turbulent boundary layer and the self-similar shear layer.

Figure 6 displays the spanwise two-point auto-correlation of u, v and p in the mixing layer at location $(x/h = 2.5,\ y/h = -0.5)$. The correlation level for the streamwise velocity decreases very quickly and tends to zero for $z/h > 0.2$. For the vertical velocity v, the correlation falls below 0.1 for $z/h > 0.6$. For the pressure, the correlation level reaches a plateau at about 0.3 for $z/h > 0.6$. This higher correlation level for the pressure than for u and v velocities is due to the acoustic waves radiated by the mixing layer. These results justify *a posteriori* that the spanwise extent of the computational domain is sufficient.

The streamwise mean velocity profiles of the mixing layer computed via LES are plotted in similarity coordinates in figure 7. The η coordinate is defined as $\eta = (y - y_c)/\delta_\omega$ where δ_ω is the vorticity thickness and y_c is the location of the velocity gradient maximum (see Jovic 1996). For $x/h \geqslant 2$ and $\eta \geqslant 0$, all the curves collapse reasonably well which implies that the streamwise velocity has reached its similarity state. The differences that occur for $x/h \geqslant 2$ and $\eta < -0.5$ are due to the ramp shape.

Figure 7 also displays the profiles of Reynolds stresses in similarity coordinates. At the beginning of the mixing layer, the Reynolds stresses decrease from the initial high values of the boundary layer to classical mixing layer values: $u_{rms}^2/\Delta U^2$ decreases for $1 \leqslant x/h < 2$ and $\overline{u'v'}/\Delta U^2$ decreases for $1 \leqslant x/h < 2.5$. Then, they increase up to the reattachment point. On the other hand, $v_{rms}^2/\Delta U^2$ increases for $1 \leqslant x/h < 1.5$,

https://doi.org/10.1017/S0022112006003995 Published online by Cambridge University Press

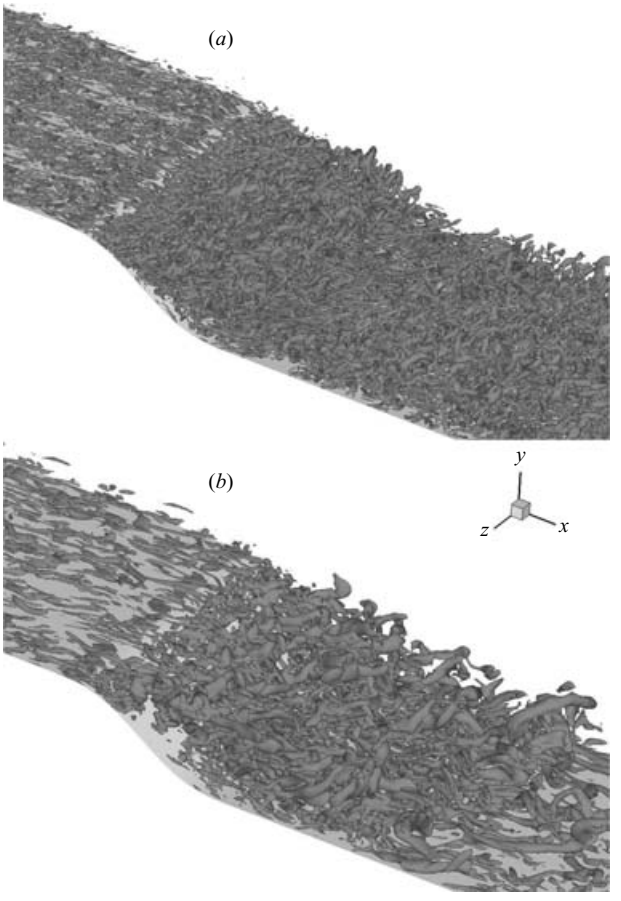


FIGURE 5. Q-criterion isosurface $Q = 4U_\infty^2/h^2$: (*a*) DNS, (*b*) LES.

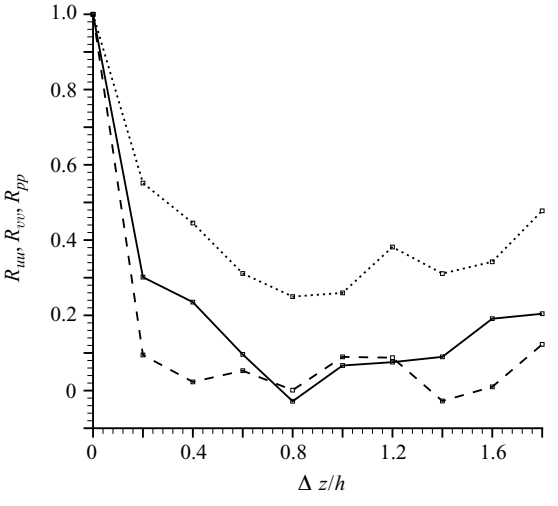


FIGURE 6. Spanwise two-point auto-correlation of u (solid line), v (dashed line) and p (dotted line) at location $x/h = 2.5$, $y/h = -0.5$ in the mixing layer.

https://doi.org/10.1017/S0022112006003995 Published online by Cambridge University Press

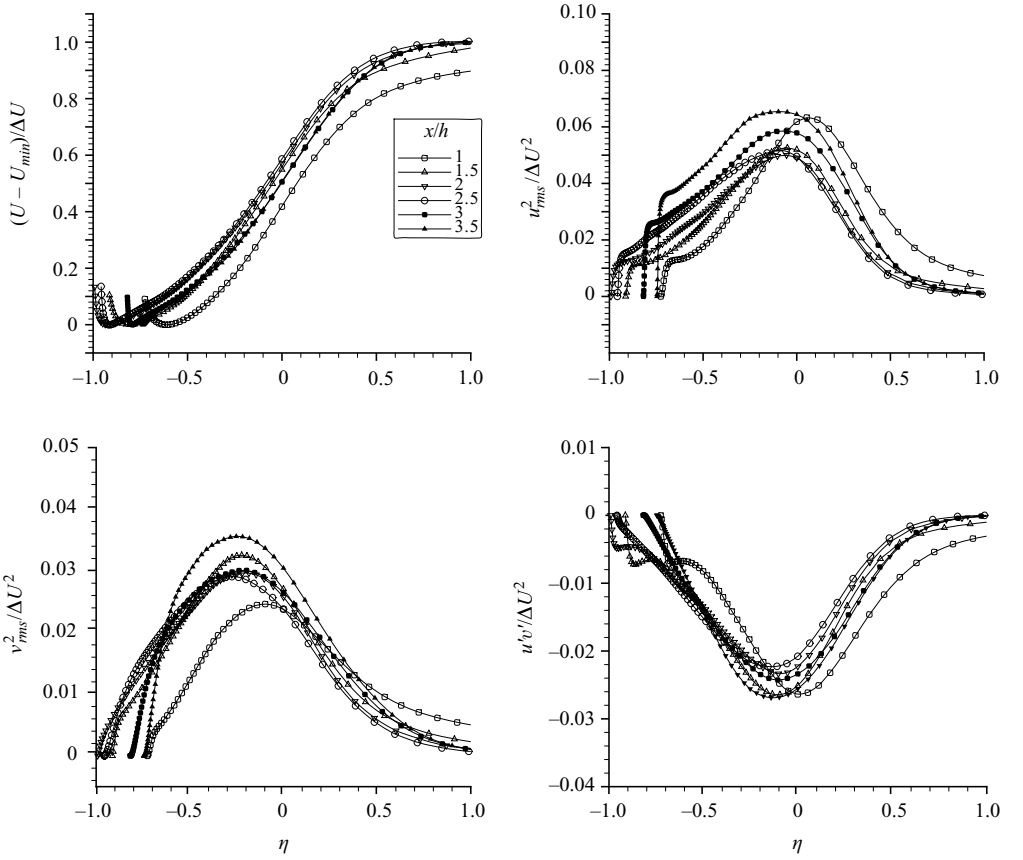


FIGURE 7. Time-averaged streamwise velocity $(U - U_{min})/\Delta U$, $u^2_{rms}/\Delta U^2$, $v^2_{rms}/\Delta U^2$ and $\overline{u'v'}/\Delta U^2$ Reynolds stress profiles of the mixing layer in similarity coordinates for the LES.

Authors	Type	$u^2_{rms}/\Delta U^2$	$v^2_{rms}/\Delta U^2$	$\overline{u'v'}/\Delta U^2$
Ruderich & Fernholz (1986)	M	0.025	0.025	0.01
Oster & Wygnanski (1982)	M	0.032	0.023	0.013
Castro & Haque (1987)	F	0.06	0.06	0.025
Jovic (1996)	BFS	0.04	0.022	0.015
Chandrsuda & Bradshaw (1981)	BFS	0.03	0.015	0.011
Friedrich & Arnal (1990) (LES)	BFS	0.05	0.020	0.016
Present case (LES)	BFS	0.065	0.036	0.026

TABLE 2. Normal and shear stress maximum level for mixing layer (M), backward-facing step (BFS) and fence flows (F).

decreases for $1.5 \leqslant x/h < 2.5$ and then increases up to the reattachment point. Table 2 gives the maximum level of normal and shear stresses observed in the literature for free mixing layers, backward-facing step flows and flows behind a fence, compared to the present case (LES). In their experiment on a separated shear layer behind a flat plate normal to the flow, Castro & Haque (1987) have observed that normal stresses are always higher than in a plane mixing layer. Here, the maximum level of

https://doi.org/10.1017/S0022112006003995 Published online by Cambridge University Press

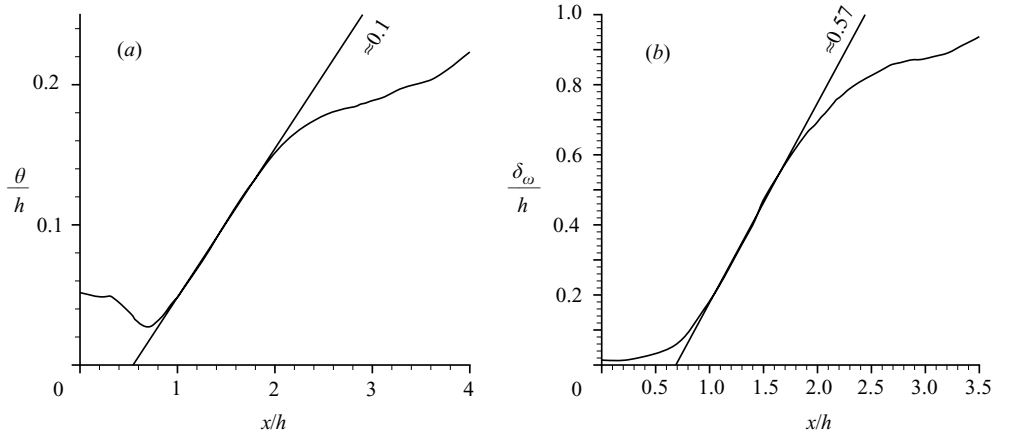


FIGURE 8. (*a*) Momentum thickness θ/h and (*b*) vorticity thickness δ_ω/h evolution along the mixing layer for the LES.

$u_{rms}^2/\Delta U^2$ is close to the value found by Castro & Haque (1987) but higher than in the experiments of Jovic (1996) and Chandrsuda & Bradshaw (1981). The maximum level of $v_{rms}^2/\Delta U^2$ is also higher than in the experiments of Jovic (1996) and Chandrsuda & Bradshaw (1981) but lower than in the experiment of Castro & Haque (1987). So, the two levels found here are higher than in previous experiments on backward-facing step flows, perhaps because of the present ramp geometry. The backflow velocity is higher and the separation bubble is thinner than for backward-facing step flows.

The maximum value of the shear stress $-\overline{u'v'}/\Delta U^2$ (figure 7) is also close to the value found by Castro & Haque (1987) but higher than in the experiments of Jovic (1996) and Chandrsuda & Bradshaw (1981).

The mixing layer streamwise evolution can be analysed by computing the momentum and vorticity thicknesses (see figure 8). Note that the incompressible momentum thickness has been used here because the ratio of the maximum to the minimum density is as low as 1.037. Because of the strong backflow velocity amplitude (16 % of U_∞), this reverse flow has been taken into account in the definition of the two thicknesses.

The momentum thickness is defined

$$\theta(x) = \int_{y_{min}}^{+\infty} \frac{\bar{u}(x,y) - u_{min}(x)}{U_\infty - u_{min}(x)} \left(1 - \frac{\bar{u}(x,y) - u_{min}(x)}{U_\infty - u_{min}(x)}\right) \mathrm{d}y \tag{4.1}$$

with $\bar{u}(x,y)$ the time-averaged and spanwise-averaged streamwise velocity and $u_{min}(x) = \min_{[y]}(\bar{u}(x,y))$.

In their experiment of free mixing layers, Browand & Troutt (1985) found that the growth rate of the momentum thickness was accurately fitted by

$$\frac{\mathrm{d}\theta}{\mathrm{d}x} = 0.034R \tag{4.2}$$

with

$$R = \frac{\Delta U}{2\overline{U}} = \frac{U_\infty - u_{min}(x)}{U_\infty + u_{min}(x)}$$

the velocity ratio. As the velocity ratio varies between 1.22 and 1.36 for $1 \leqslant x/h \leqslant 2$ in our case, $\mathrm{d}\theta/\mathrm{d}x$ should be equal to 0.041–0.046 according to relation (4.2). Here,

https://doi.org/10.1017/S0022112006003995 Published online by Cambridge University Press

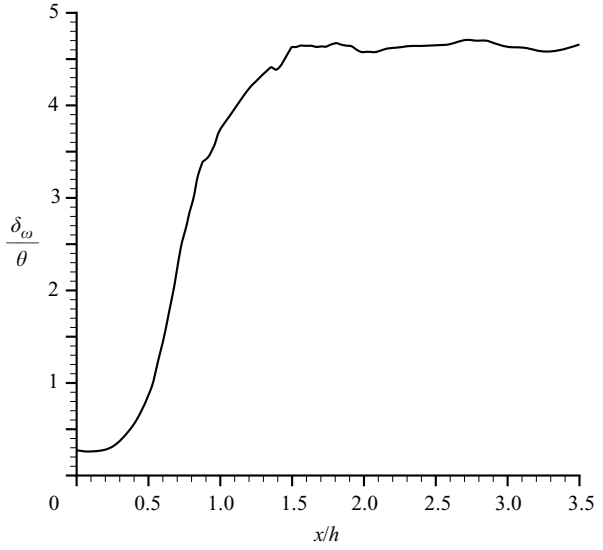


FIGURE 9. Ratio between vorticity thickness δ_ω and momentum thickness θ along the mixing layer.

the growth rate (equal to 0.1) is more than twice the value expected for a free mixing layer. This is due to the recirculation of the turbulent structures which are reabsorbed into the mixing layer.

The vorticity thickness is defined

$$\delta_\omega(x) = \frac{U_\infty - u_{low}(x)}{\max_{[y]}\left(\dfrac{\partial \bar{u}(x,\, y)}{\partial y}\right)}. \tag{4.3}$$

For the vorticity thickness (figure 8*b*), two regions can be observed in the mixing layer as in Larchevêque *et al.* (2004). The first one, located between $x/h = 0$ and $x/h = 1$, exhibits a large growth rate. This growth is exponential as predicted by linear stability theory. The second region is wider with a constant growth rate equal to 0.57. Browand & Troutt (1985) give a growth rate

$$\frac{\mathrm{d}\delta_\omega}{\mathrm{d}x} = 0.17R. \tag{4.4}$$

As the velocity ratio varies between 1.22 and 1.36 for $1 \leqslant x/h \leqslant 2$, $\mathrm{d}\delta_\omega/\mathrm{d}x$ should be equal to 0.2–0.23. For the momentum thickness, the growth rate (equal to 0.57) is more than twice the expected value in a free mixing layer. The present shear layer differs from the canonical plane mixing layer by the fact that the low-speed-side flow is highly turbulent as opposed to the low-turbulence-level stream in a plane mixing layer. Jovic (1996) and Castro & Haque (1987) have also reported a higher growth rate in their experiments.

The ratio between the momentum and vorticity thicknesses is shown in figure 9. It is noteworthy that this ratio reaches a constant value close to 4.5 for $x/h \geqslant 1.5$. Moreover, Castro & Haque (1987) and Larchevêque *et al.* (2004) have observed for their mixing layers that the ratio between the spreading rates of the momentum and vorticity thicknesses has a value close to 5. With a ratio of the growth rates of 5.7, the present computation is close to this observed value.

https://doi.org/10.1017/S0022112006003995 Published online by Cambridge University Press

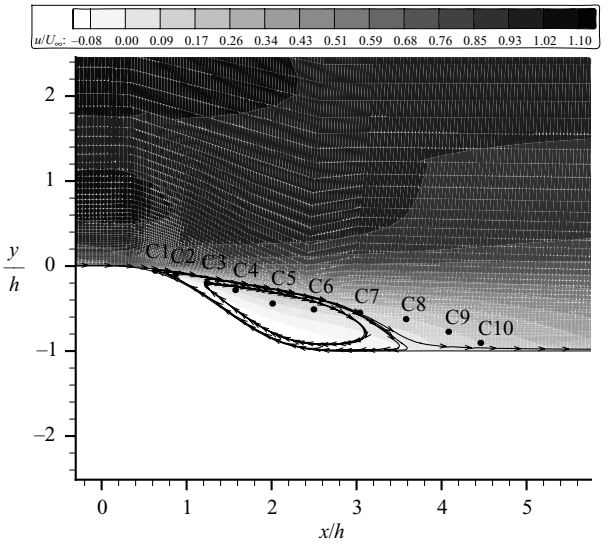


FIGURE 10. Mean streamwise velocity field showing locations of the pressure sensors in the mixing layer.

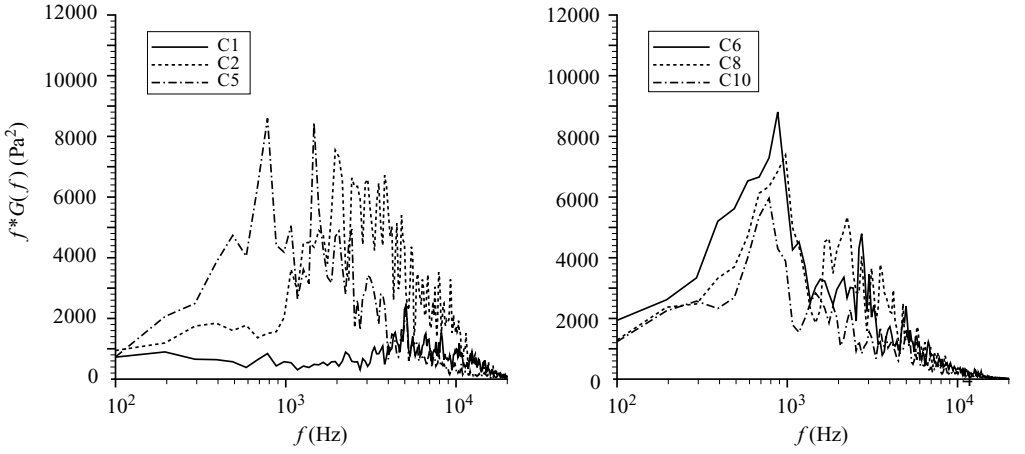


FIGURE 11. LES pressure spectra along the mixing layer for six sensors (C1, C2, C5, C6, C8 and C10).

Figure 10 presents the locations of ten sensors, referred to as C1 to C10, from which pressure spectra are computed. These spectra are shown in figure 11 for six of the sensors. The length of time records in the LES is 0.0836 s, the sampling frequency is 200 kHz, the number of overlapping blocks is 15, which results in a 97 Hz resolution frequency. At the beginning of the shear layer, i.e. at sensors C1 and C2, a broadband spectrum corresponding to the shear layer roll-up is observed. As will be shown in figure 32, the Kelvin–Helmholtz frequencies observed in these spectra are close to the most amplified frequencies computed via to a linear inviscid stability analysis. Further downstream, for sensor C5, two distinct peaks are present: one around 1600 Hz ($F^+ = 1.14 \pm 0.07$) and a second at half the previous frequency ($F^+ = 0.57 \pm 0.07$). The second peak is close to the range of the expected shedding

https://doi.org/10.1017/S0022112006003995 Published online by Cambridge University Press

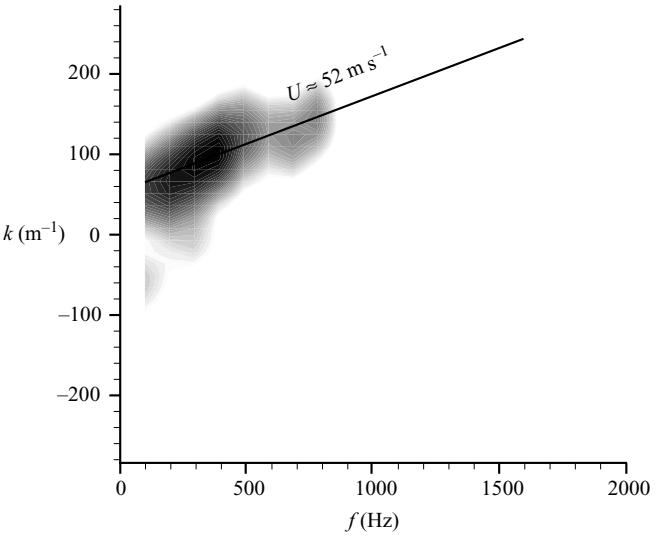


FIGURE 12. LES frequency–wavenumber pressure spectra estimator $\Psi(f,k)$ for 19 sensors along the wall.

frequency ($0.6 < F^+ < 0.9$). The energy level of the first peak is larger than that of the second peak for sensors C3 to C4 while its subharmonic dominates for sensors C5 to C10. The growing subharmonic is due to vortex pairing inside the mixing layer. This vortex merging takes place near sensor C5 at $x/h = 2$. This observation is corroborated by figure 8 in which the shear layer vorticity thickness reaches a plateau for $x/h \geqslant 2$. As demonstrated by Ho & Huang (2002), the start of the plateau marks the vortex merging location. Also, a low-frequency flapping phenomenon has been reported in the experiments of Eaton & Johnston (1981), Cherry *et al.* (1984), Kiya & Sasaki (1985) and in the simulations by Yang & Voke (2001). In our case, no evidence of such a flapping of the shear layer has been found.

Figure 12 displays the LES frequency–wavenumber pressure spectra for 19 sensors uniformly distributed along the wall between the separation point and the reattachment one. The spectrum estimator $\Psi(f,k)$ is based on the cross-spectrum between the points x_i and x_j written as $S_{x_i x_j}$, and is defined

$$\Psi(f,k) = \mathrm{P}(k)^H \mathrm{M}(f) \mathrm{P}(k) \tag{4.5}$$

where H indicates the Hermitian transpose and M and P are defined

$$\mathrm{M}_{ij}(f) = S_{x_i x_j}(f), \tag{4.6}$$

$$\mathrm{P}_i(k) = \exp(\mathrm{i}kx_i). \tag{4.7}$$

Convective phenomena are identified by regions of constant ratio ω/k, where ω is the pulsation and k the wavenumber. The advantage of frequency–wavenumber spectra with respect to two-point two-time correlations is that they make it possible to distinguish between multiple convection velocities. Moreover, each convective phenomenon can be linked to a fundamental frequency. A convection velocity of $0.5U_\infty$ is clearly observed. This velocity corresponds to the signature of shear layer structures on the wall. This is the expected convection velocity of the Kelvin–Helmholtz two-dimensional structures (see table 3). Moreover, no zero convection velocity has been found and consequently there is no low-frequency flapping of the shear layer, as previously observed in the pressure spectra.

https://doi.org/10.1017/S0022112006003995 Published online by Cambridge University Press

Author	Type	Convection velocity
Brown & Roshko (1974)	M	$0.53U_\infty$
Cherry *et al.* (1984)	FP	0.5–$0.63U_\infty$
Kiya & Sasaki (1985)	FP	$0.5U_\infty$
Simpson (1989)	review	$0.6U_\infty$
Kiya *et al.* (1997)	FP	$0.5U_\infty$
Heenan & Morrison (1998)	BFS	0.5–$0.6U_\infty$
Lee & Sung (2001)	BFS	$0.6U_\infty$
Yang & Voke (2001)	FP	$0.58U_\infty$
Hudy *et al.* (2003)	F	$0.57U_\infty$
Morris & Foss (2003)	M	$0.5U_\infty$
Larchevêque *et al.* (2003)	CM	$0.65U_\infty$
Dejoan & Leschziner (2004)	BFS	$0.4U_\infty$
Larchevêque *et al.* (2004)	CM	$0.53U_\infty$
Liu *et al.* (2005)	BFS	$0.56U_\infty$
Present case	BFS	$0.5U_\infty$

TABLE 3. Shear layer vortices convection velocity for different flows (Configuration type: M = mixing layer, BFS = backward-facing step, F = fence, FP = flat-plate leading edge, CM = mixing layer past a cavity).

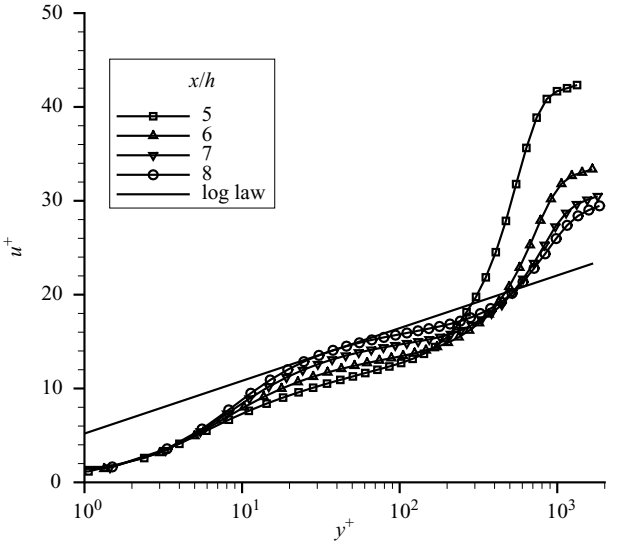


FIGURE 13. LES mean streamwise velocity profiles of the reattached flow in semi-log coordinates with 'universal' logarithmic law $U/u_\tau = (1/0.41)\ln(u_\tau y/\nu) + 5.2$.

4.3. *Recovery region*

In the recovery region, the separated shear layer impinges on a solid wall and begins to relax toward an equilibrium turbulent boundary layer. The development of this turbulent boundary layer is far from being instantaneous. In the experiment of Jovic (1996), an equilibrium state for the turbulent boundary layer is not reached before more than fifty ramp heights. At the reattachment point, the flow is dominated by mixing layer turbulent structures. Then, in the internal layer, turbulent boundary layer structures compete with mixing layer ones. Figure 13 displays the mean streamwise velocity profiles of the reattached flow in semi-log coordinates. It is apparent that the velocity profiles are far from the universal log law. The presence of a large

https://doi.org/10.1017/S0022112006003995 Published online by Cambridge University Press

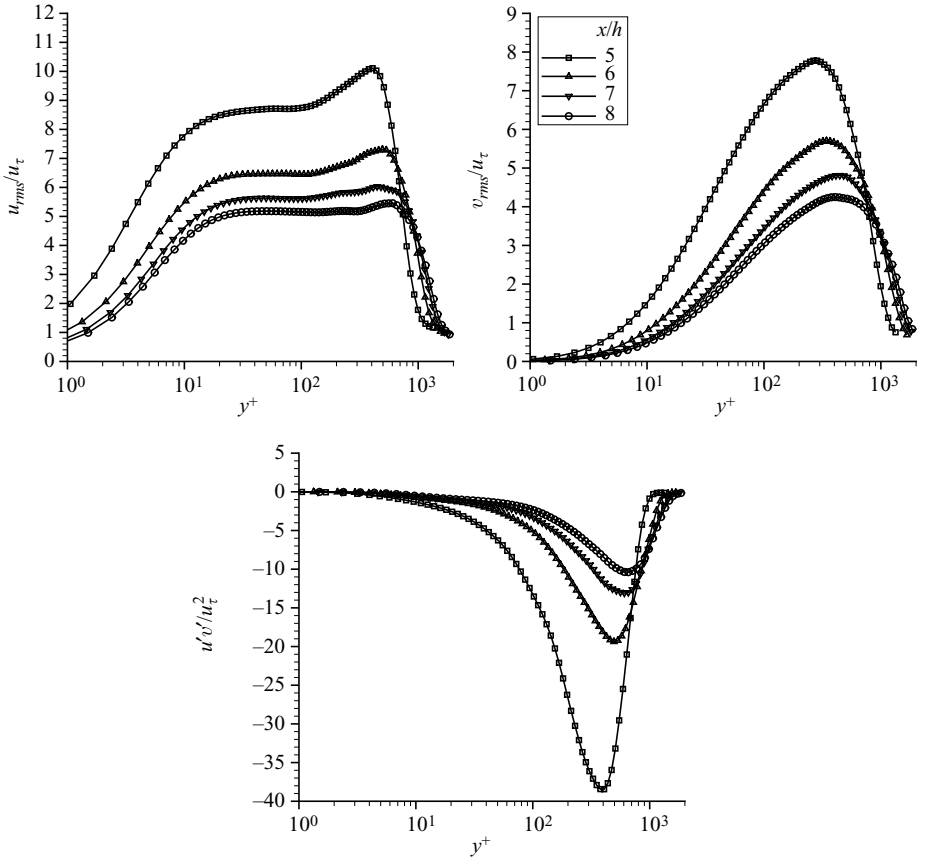


FIGURE 14. LES u_{rms}, v_{rms} and $\overline{u'v'}$ Reynolds stresses profiles of the reattached flow in semi-log coordinates.

wake zone is due to the mixing-layer-like flow near reattachment. As the turbulent boundary layer redevelops with x/h, the friction velocity increases and consequently the non-dimensionalized velocity decreases in the wake zone whereas it increases in the logarithmic zone. At the end of the computational domain, the velocity profiles still do not collapse with the logarithmic law.

Normal and shear Reynolds stress profiles are shown in figure 14. All the Reynolds stresses decrease while the boundary layer is relaxing. Downstream of reattachment, the non-dimensionalized Reynolds stresses decay rapidly as the friction velocity increases, the maximum values of u_{rms}/u_τ and v_{rms}/u_τ fall by approximately 30 % and the maximum value of $\overline{uv}/u_\tau^2$ is halved between $x/h = 5$ and $x/h = 6$. For the backward-facing step flow of Jovic (1996), the u_{rms} profile exhibits a plateau where $u_{rms}/u_\tau \simeq 4.5$ for $20 < y^+ < 300$. The plateau region is broader and propagates away from the wall with downstream distance. Jovic (1996) interpretes this plateau as a region where the wall and the external layer influences overlap. As the recovering boundary layer thickens, this region moves away from the wall. The plateau region can be identified as the limit between two distinct layers: the internal boundary layer and the outer layer which is characterized by a strong memory effect of the mixing-layer type of Reynolds stress production.

In summary, a comparison between the DNS and the LES mean velocities and Reynolds stress profiles has demonstrated the capability of LES to accurately predict

https://doi.org/10.1017/S0022112006003995 Published online by Cambridge University Press

the present separated flow. The Reynolds stress maximum levels are a little higher than in the backward-facing step flow, a fact which can be explained by the thinner separation bubble in the present case. The momentum and vorticity thicknesses are higher than for a free mixing layer because of the recirculation and re-entrainment of vorticity at the separation point. The next part will be devoted to the study of the controlled flow.

5. Controlled flows

The reduced frequency and momentum coefficient are the two most important non-dimensional parameters for separation control by periodic oscillations. The reduced frequency is defined

$$F^+ = fL/U_\infty. \tag{5.1}$$

Here, $L = 3.45h$ is the separation length without control computed from DNS. Two synthetic jet frequencies have been considered: $F^+ = 0.5$ ($f = 720$ Hz, $St_h = 0.14$, $St_{\theta_0} = 0.007$ with $\theta_0 = 0.05h$ the incoming boundary layer momentum thickness) and $F^+ = 4$ ($f = 5800$ Hz, $St_h = 1.1$, $St_{\theta_0} = 0.057$).

The reduced frequency value $F^+ = 0.5$ has been reported to be the most effective in previous papers (Brunn & Nitsche 2003; Narayanan & Banaszuk 2003; Kiya, Shimizu & Mochizuki 1997) and in two-dimensional unsteady Reynolds-averaged Navier–Stokes simulations with the Spalart–Allmaras turbulence model (not shown here). This frequency is close to the shedding mode frequency $F^+ = 0.57$ found in the pressure spectra of the uncontrolled flow (figure 11).

The $F^+ = 4$ actuation frequency has been chosen to study the effect of high-frequency forcing control. The purpose here is twofold. The first is to study the 'virtual aeroshaping effect' discussed by Amitay & Glezer (2002) and Glezer *et al.* (2005). These authors observed that forcing at a frequency $F^+ = O(10)$ is able to suppress separation without the drawback of increasing the lift fluctuation level as in the low-frequency control case. The second goal is to investigate the large-scale fluctuation level decrease as observed by Stanek *et al.* (2000, 2002*b*). The low- and high-frequency forcing cases will be hereafter denoted LF and HF, respectively.

The momentum coefficient is defined

$$C_\mu = \frac{\rho_j d U_j^2}{\rho_\infty L U_\infty^2} \tag{5.2}$$

with d the actuator slot width, and U_j the synthetic jet velocity at the orifice. For the two controlled cases, the momentum coefficient C_μ is 1 % which gives a velocity ratio between the synthetic jet and the crossflow equal to 0.5. In our case, the synthetic jet maximum velocity is $50\,\mathrm{m\,s^{-1}}$ which is a reasonable value for current actuators.

One important parameter for the synthetic jet is the non-dimensionalized stroke length L_0/d defined

$$L_0 = \int_0^{T/2} \widetilde{u}(t)\,\mathrm{d}t \tag{5.3}$$

where $\widetilde{u}(t)$ is the velocity averaged on the orifice surface and T the synthetic jet period.

This stroke length can be expressed as a function of the jet Strouhal number:

$$\frac{L_0}{d} = \frac{U_0}{f.d} = \frac{1}{St_0} \tag{5.4}$$

https://doi.org/10.1017/S0022112006003995 Published online by Cambridge University Press

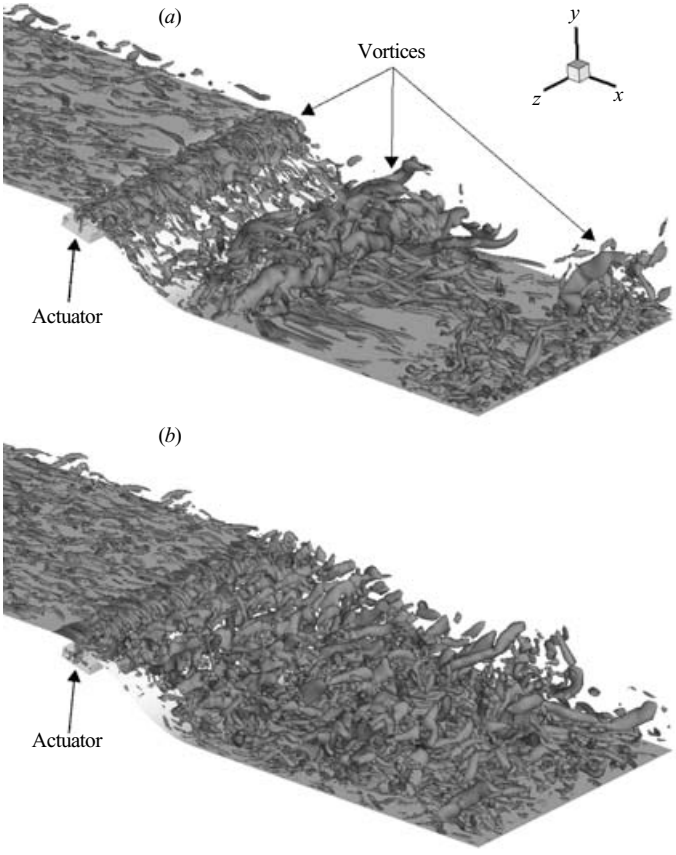


FIGURE 15. Q-criterion isosurface $Q = 4U_\infty^2/h^2$: (*a*) LF case, (*b*) HF case.

where U_0 is defined as L_0/T. This last equation shows that the non-dimensionalized stroke length is the inverse of the jet Strouhal number.

A synthetic jet is formed if the vortex pair or ring formed during blowing is not reabsorbed during suction. A jet formation criterion is that the non-dimensionalized stroke length for a two-dimensionnal slot must be larger than 3 for a synthetic jet in quiescent air (Holman *et al.* 2005) and larger than 2 in a boundary layer (Shuster *et al.* 2005). Here, for the LF forcing L_0/d is equal to 6.3 whereas it is equal to 0.78 for the HF forcing. So, according to the criterion of Shuster *et al.* (2005), a synthetic jet should not form in the HF case but as will be shown in the following, the actuator still has a significant effect on the flow.

In the following section, the reduced frequency effect on the separated flow is studied using the LES which has been validated in the first part of the paper.

5.1. *Instantaneous flow*

A comparison of the instantaneous turbulent structures for the two controlled cases is displayed in figure 15. In the LF case, the actuation has strongly modified the flow by generating spanwise vortex. The flow seems to be reattached between each vortex. On the other hand, the HF forcing effect on the flow is less visible.

https://doi.org/10.1017/S0022112006003995 Published online by Cambridge University Press

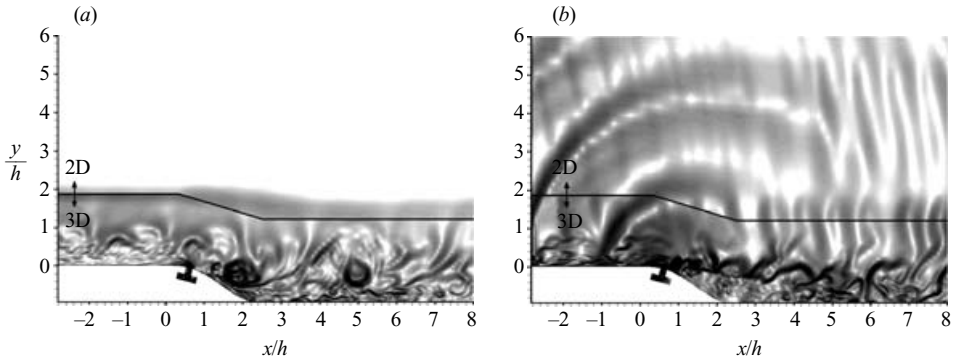


FIGURE 16. Instantaneous pseudo-schlieren visualization at the same instant as figure 15: (*a*) LF case, (*b*) HF case.

Instantaneous pseudo-schlieren visualizations for the two controlled cases are shown in figure 16. These visualizations are obtained by the computation of $||\mathrm{grad}\rho||$:

$$Sch(x, y) = \sqrt{\left(\frac{\partial \rho}{\partial x}\right) + \left(\frac{\partial \rho}{\partial y}\right)}. \tag{5.5}$$

In the LF case, spanwise vortices are visible near the actuator location and at $x/h = 2$ and 5. The mixing layer has been replaced by series of downstream-travelling large spanwise vortices. Noteworthy in the HF case is the presence of acoustic waves created by the actuator. It is easy to verify that the acoustic wave frequency is equal to the forcing frequency since the wavelength is approximately equal to $2h$ upstream of the actuator and the sound velocity is equal to $U_\infty - c = 101 - 337 = -236\,\mathrm{m\,s^{-1}}$ so $f = 236/(2 \times 0.02) \simeq 5800\,\mathrm{Hz}$. Moreover, the Kelvin–Helmholtz vortices of the mixing layer are clearly visible.

In summary, examination of these instantaneous visualizations suggests that the acoustic contribution is important in the HF case whereas the LF actuation produces essentially vorticity.

5.2. *Mean flow*

The mean streamwise velocity field is displayed in figure 17 with streamlines showing the extent of the separation bubble. The separation bubble is almost suppressed in the LF case and is thinner than in the uncontrolled case. On the other hand, the separation bubble size in the HF forcing case is dramatically increased. There is a small low-velocity zone on the windward edge of the jet but the flow remains attached between $x/h = 0.5$ and $x/h = 0.9$ (see figure 18). So the increase of the separation length for the HF case is not due to an earlier separation and no blockage effect of the jet can be found. Nevertheless the actuation thickens the boundary layer and we can anticipate that the stability properties of the mean velocity field are affected by such a forcing. The use of the previous synthetic jet formation criterion of Shuster *et al.* (2005) is not relevant to the present case because even if a synthetic jet were not to form in our case, it is obvious here than the actuation has a strong effect on separation.

The forcing effect on the mean streamwise velocity u and its fluctuations u_{rms} is shown in figures 19 and 20, respectively. At $x/h = 2$, the backflow velocity amplitude is lower in the LF case and higher in the HF case than in the baseline case. The maximum backflow velocity is equal to 16 % of U_∞ for the uncontrolled flow, 9 % of

https://doi.org/10.1017/S0022112006003995 Published online by Cambridge University Press

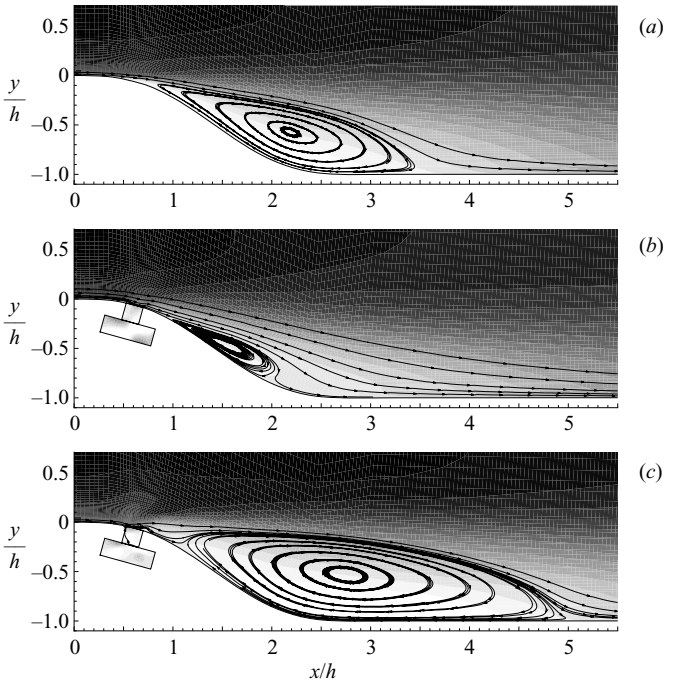


FIGURE 17. Mean streamwise velocity field and streamlines showing the extent of the separation bubble: (*a*) uncontrolled flow, (*b*) LF case and (*c*) HF case.

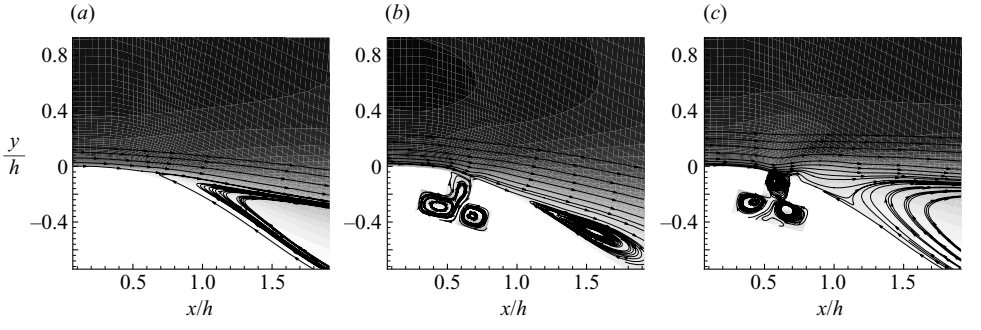


FIGURE 18. Time-averaged streamwise velocity field close to the separation point: (*a*) uncontrolled flow, (*b*) LF case and (*c*) HF case.

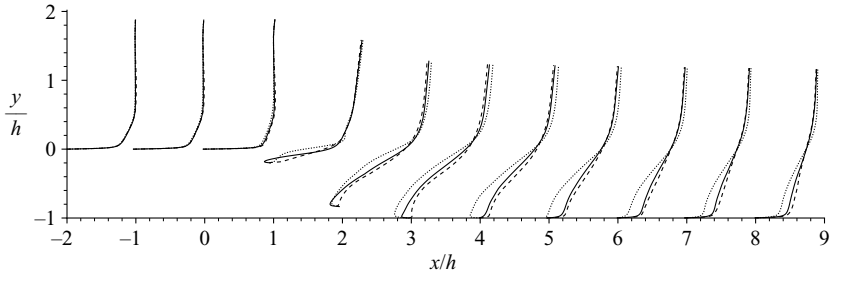


FIGURE 19. Time-averaged streamwise velocity $x/h + u/U_\infty$ for the three cases: uncontrolled flow (solid line), LF case (dashed line) and HF case (dotted line).

https://doi.org/10.1017/S0022112006003995 Published online by Cambridge University Press

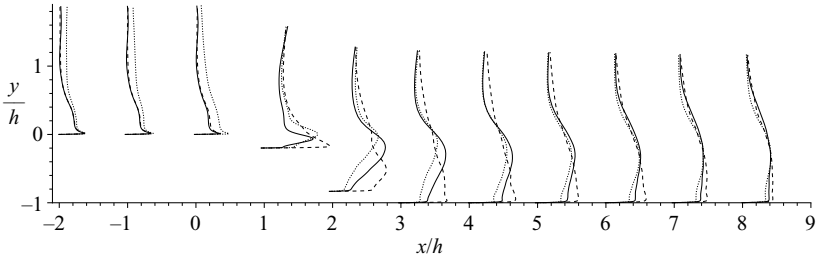


FIGURE 20. Time-averaged streamwise velocity fluctuations $x/h + u_{rms}/40$ for the three cases: uncontrolled flow (solid line), LF case (dashed line) and HF case (dotted line).

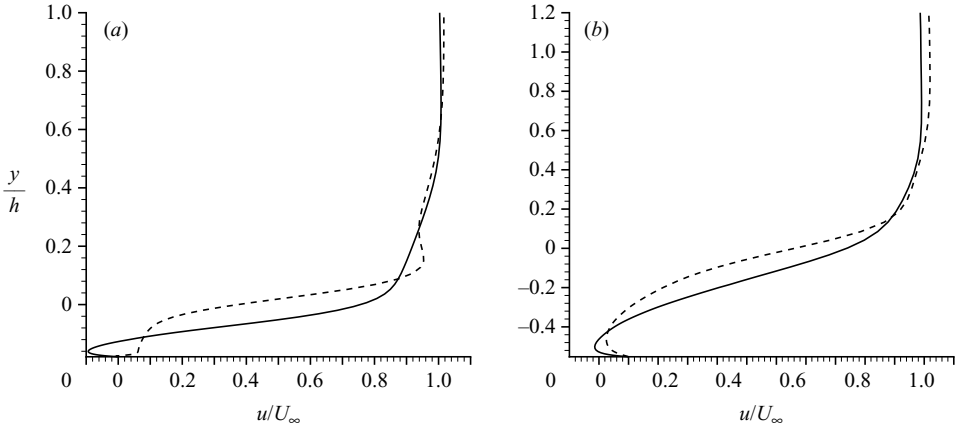


FIGURE 21. Time-averaged streamwise velocity profile for the uncontrolled flow (solid line) and the HF case (dashed line) at (*a*) $x/h = 0.9$ and (*b*) $x/h = 1.6$ locations.

U_∞ for the LF case and 21 % for the HF case. Downstream of $x/h = 3$, the boundary layer in the LF case redevelops earlier than in the uncontrolled case near the wall.

Figure 21 displays a closer view of the mean streamwise velocity near $x/h = 0.9$ (*a*) and $x/h = 1.6$ (*b*). The HF forcing modifies the inflection point of the velocity profile compared to the uncontrolled case. As observed by Stanek *et al.* (2002*a*), there are four inflection points in the HF forcing case at $x/h = 0.9$ (*a*). According to Fjortoft's theorem (Huerre & Rossi 1998), if y_0 is the position of the inflection point ($\mathrm{d}^2U(y_0)/\mathrm{d}y^2 = 0$), then a necessary (but not sufficient) condition for an inviscid instability to exist is that $(\mathrm{d}^2U(y)/\mathrm{d}y^2)(U(y) - U(y_0)) < 0$ for some y. The nearest inflection point from the wall ($y/h = -0.016$) is stable according to Fjortoft's theorem whereas the second one ($y/h = 0$) is unstable. The third and fourth inflection points ($y/h = 0.2; 0.44$) are associated with low streamwise velocity vertical gradient so their influence on the development of the perturbations in the mixing layer is weak. The unique inflection point of the uncontrolled case is also unstable. The stability of the first inflection point in the HF case is used by Stanek *et al.* (2002*a*, *b*) to explain the lower energy level of the large scales. However, at the $x/h = 1.6$ location (see figure 21*b*), there is only one inflection point in both cases. A stability study of the velocity profiles is required to draw conclusions on the stability properties of the HF forcing flow.

https://doi.org/10.1017/S0022112006003995 Published online by Cambridge University Press

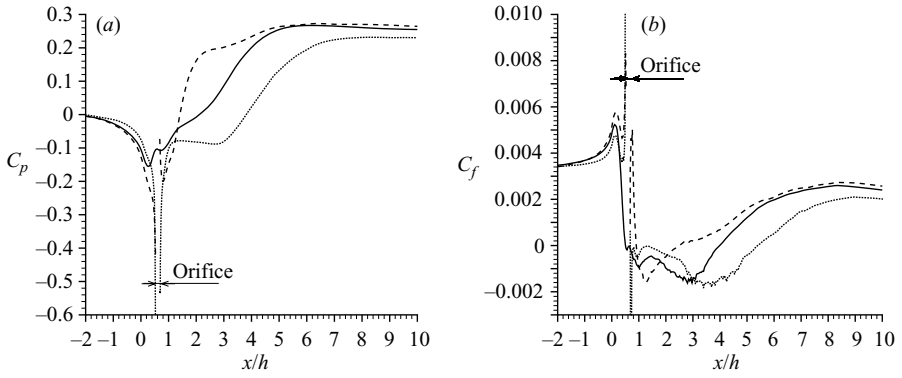


FIGURE 22. Surface pressure coefficient C_p (*a*) and skin-friction coefficient C_f (*b*) for the three cases: uncontrolled flow (solid line), LF case (dashed line) and HF case (dotted line).

From figure 20, one can observe that, in the actuator vicinity at $x/h=0$ and $x/h=1$, the level of streamwise velocity fluctuations of the two controlled cases is higher than in the uncontrolled case.

In the LF case, downstream of the reattachment, the u_{rms} level is higher than in the baseline case near the wall because of the earlier boundary layer redevelopment. These results differ from those of Neumann & Wengle (2004*b*) who report a lower level of u_{rms} in the controlled case downstream of reattachment. This may be due to the higher level of excitation in the present case ($U_j/U_\infty=0.5$ instead of 0.2).

In the HF case u_{rms} is lower than in the uncontrolled case at all positions downstream of the reattachment point. Unlike the uncontrolled and LF cases, u_{rms} is higher upstream of the actuator. At high frequency, the synthetic jet operates in an *acoustic-radiation mode* as reported by Ingard (1953). High-amplitude sound waves are created by the diaphragm oscillations at the bottom of the cavity and propagate in all directions. These waves interact with the vortical velocity field to produce velocity fluctuations. On the other hand, the LF case corresponds to the *synthetic jet mode* according to the Ingard's classification, in which the main mechanism is vorticity generation. Nevertheless, it is worth noting that in both controlled cases the sound pressure level (in the whole computational domain) is higher than in the uncontrolled case.

Figure 22 displays the surface pressure coefficient $C_p=(p_\infty-p)/(0.5\rho_\infty U_\infty^2)$ and the skin-friction coefficient C_f for the three cases. The separation points are $x_s/h=0.91$ for the LF case and $x_s/h=0.68$ for the HF case. The reattachment points are $x_r/h=2.49$ for the LF case and $x_r/h=5.39$ for the HF case. The separation length is reduced by 54 % for the LF case at $F^+=0.5$. The increase of the separation length by 43 % for the HF case is not due to the earlier separation because the separation process is delayed for the two controlled cases. The effect of the actuator cavity was investigated by LES with the actuator cavity but without the forcing. The results show that the separation length is nearly the same as in the baseline case ($L=3.49h$ with the cavity and $3.45h$ without it). The mean streamwise velocity field with and without the cavity is displayed in figure 23. There are only weak differences in the separation bubble between the two cases which explains the slightly different separation length. Therefore the effect of the actuation is not due only to the presence of the actuator cavity but also to the synthetic jet generated by the diaphragm oscillations.

https://doi.org/10.1017/S0022112006003995 Published online by Cambridge University Press

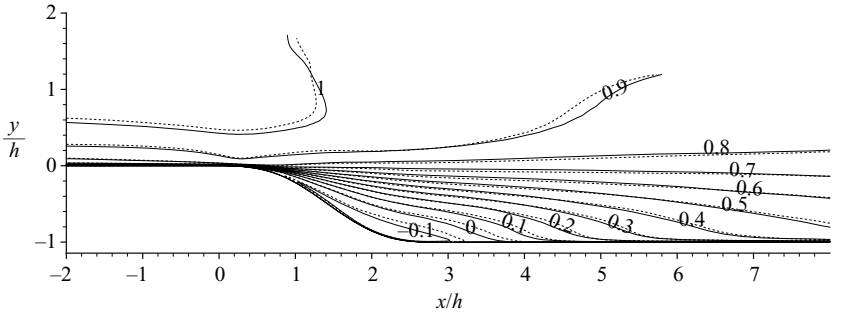


FIGURE 23. Mean streamwise velocity field: uncontrolled flow without the cavity (solid line) and with the cavity (dashed line).

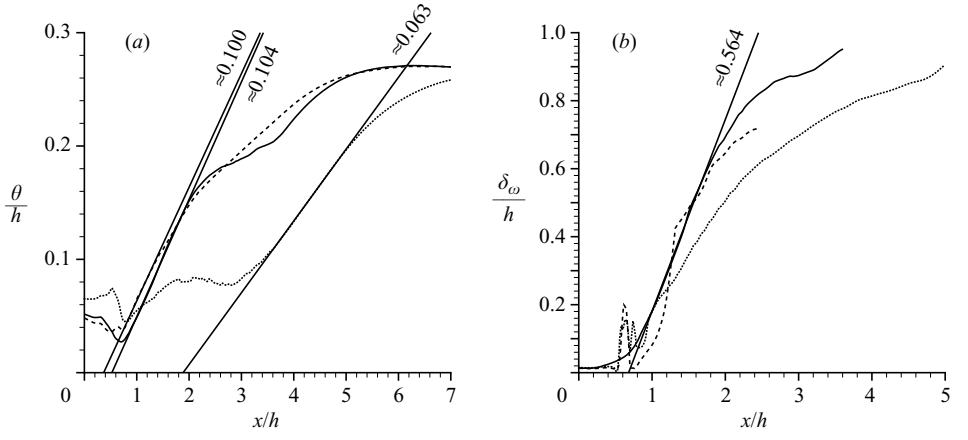


FIGURE 24. (*a*) Momentum thickness θ and (*b*) vorticity thickness δ_ω evolution along the mixing layer: uncontrolled flow (solid line), LF case (dashed line) and HF case (dotted line).

It is clear that the synthetic jet frequency has a strong effect on the pressure distribution. The pressure plateau characteristic of separated flows is only apparent in the HF case pressure distribution. In the LF case, both lift and drag are lower than in the uncontrolled case whereas in the HF case, the opposite is observed.

Figure 24(*a*) shows that the momentum thickness growth rates in the uncontrolled case and in the LF forcing case are nearly identical with $\mathrm{d}\theta/\mathrm{d}x \simeq 0.1$. For the HF case, the momentum thickness remains nearly constant between $x/h = 1.5$ and 2.8. The momentum and vorticity thicknesses in the uncontrolled and LF cases are nearly identical. The effect of the HF forcing is a reduction of the momentum and vorticity thicknesses growth rates.

Figure 25 details the effect of the forcing frequency on the mean spanwise vorticity. Despite the spanwise vorticity source provided by the actuator, the level for the LF case is nearly equal to that for the uncontrolled case but its maximum is closer to the wall. This is due to the spanwise vortices formed during the actuator blowing phase being convected along the wall. As the separation has been delayed to $x/h = 0.91$, there is a higher vorticity level for $0.5 \leqslant x/h \leqslant 1.2$ close to the wall corresponding to higher friction. In the HF case, the spanwise vorticity level is higher than in the two other cases but the mixing layer is deflected away from the wall so less high-momentum fluid is carried towards the wall.

https://doi.org/10.1017/S0022112006003995 Published online by Cambridge University Press

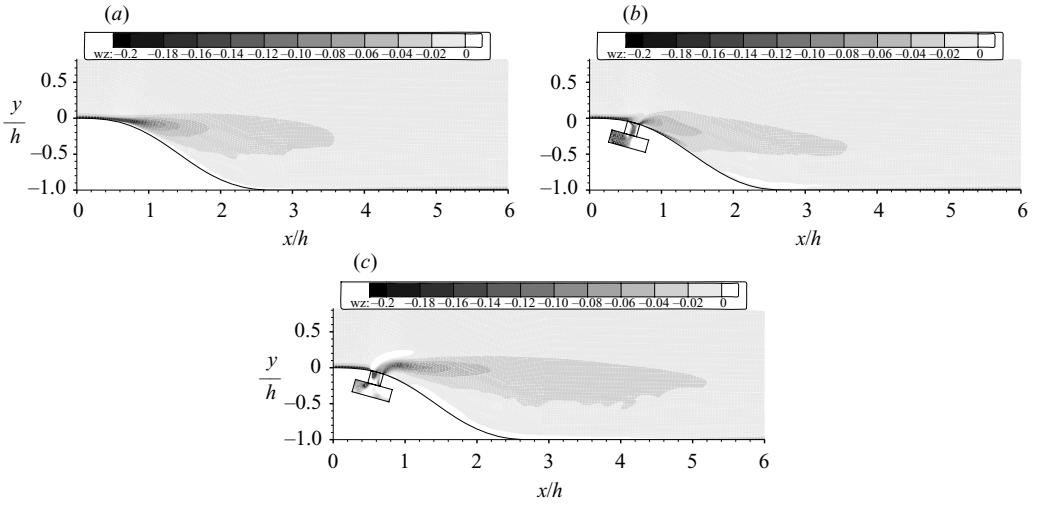


FIGURE 25. Forcing frequency effect on the mean spanwise vorticity ω_z. (*a*) Uncontrolled case, (*b*) LF case, (*c*) HF case.

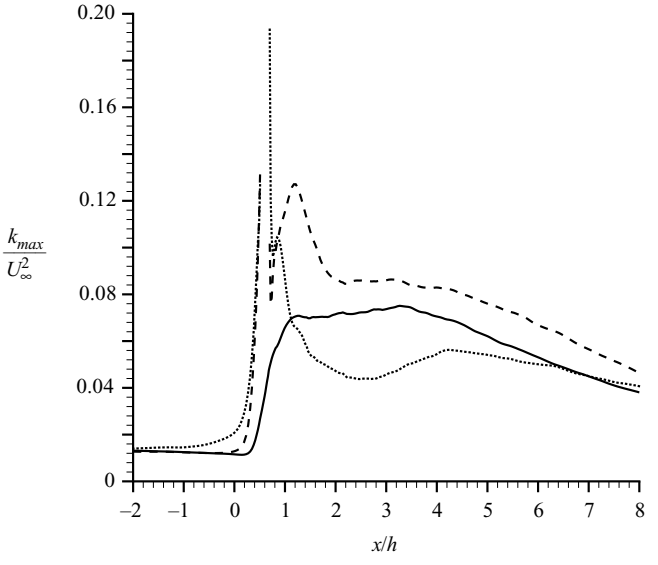


FIGURE 26. Turbulent kinetic energy k along the line of its maxima for the three cases: uncontrolled flow (solid line), LF case (dashed line) and HF case (dotted line).

The streamwise evolution of the maximum of turbulent kinetic energy (TKE) is displayed in figure 26. Unlike to the LF forcing, the HF forcing induces a decrease of the turbulent kinetic energy level for $1 \leqslant x/h \leqslant 6$. For example, at $x/h = 3$, the TKE level is 17 % higher in the LF case than in the uncontrolled case whereas it is 38 % smaller in the HF case. In both controlled cases, one can observe a TKE peak downstream of the actuator. This peak is closer to the actuator location for the HF case ($x/h = 0.8$) than for the LF case $x/h = 1.2$ since the forcing wavelength is smaller for the HF case than for the LF case.

https://doi.org/10.1017/S0022112006003995 Published online by Cambridge University Press

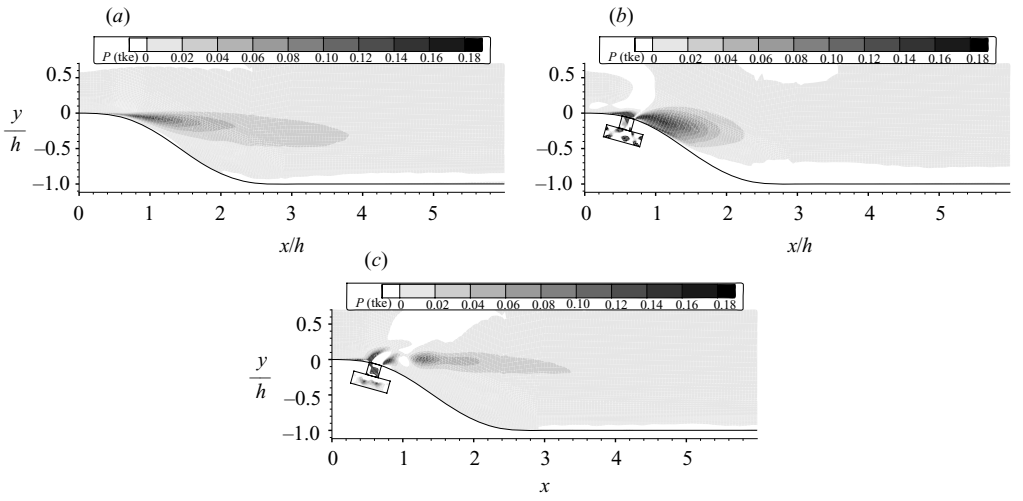


FIGURE 27. Forcing frequency effect on the turbulent kinetic energy production $P/(U_\infty^3/h)$. (*a*) Uncontrolled case, (*b*) LF case, (*c*) HF case.

Figure 27 shows the spatial distribution of the turbulent kinetic energy production term, defined

$$P = -\overline{u'^2}\frac{\partial \bar{u}}{\partial x} - \overline{v'^2}\frac{\partial \bar{v}}{\partial y} - \overline{u'v'}\left(\frac{\partial \bar{u}}{\partial y} + \frac{\partial \bar{v}}{\partial x}\right). \tag{5.6}$$

The analysis is restricted to the production term since it is the main contributor to the TKE budget. Scarano, Benocci & Riethmuller (1999) observed that vortex roll-up takes place in regions of high TKE production. In the LF case, the level of TKE production is twice that in the uncontrolled case and three times higher than in the HF case. In this latter case, the TKE production is negative in the synthetic jet and at $x/h = 1$ whereas it is positive on its upstream and downstream edges. In summary, the effect of the low-frequency forcing is an increase of the TKE production in contrast to the high-frequency forcing.

5.3. *Spectral analysis*

The frequency–wavenumber pressure spectra for the three cases are shown in figure 28. The mean convection velocity measured between the ten sensors is $0.5U_\infty$ for the uncontrolled case, $0.33U_\infty$ for the LF case and $320\,\mathrm{m\,s^{-1}}$ for the HF case.

The convection speed of the LF case is lower than in the uncontrolled case because of the larger circulation of the vortices formed by the actuation. The mean velocity between sensors C1 and C10 is $13\,\mathrm{m\,s^{-1}}$. The sound velocity $u+c$ is $13+337=350\,\mathrm{m\,s^{-1}}$ with c the sound velocity in the flow frame of reference. The $320\,\mathrm{m\,s^{-1}}$ convection speed found with the frequency–wavenumber pressure spectra in the HF case is in acceptable agreement with sound velocity considering the uncertainty of the estimator. This, together with the instantaneous pressure field shown in figure 16, confirms that, in the HF case, the synthetic jet operates in an acoustic-dominated mode.

Figure 29 presents the pressure spectra for four sensors C1, C3, C5 and C10. The fundamental and the harmonics of the forcing frequency for the two controlled cases are clearly identified. There is a locking of the shear layer at the forcing frequency in the two controlled case, but no subharmonics of the forcing frequency are detected. This demonstrates the absence of vortex merging in the two controlled cases. Owing

https://doi.org/10.1017/S0022112006003995 Published online by Cambridge University Press

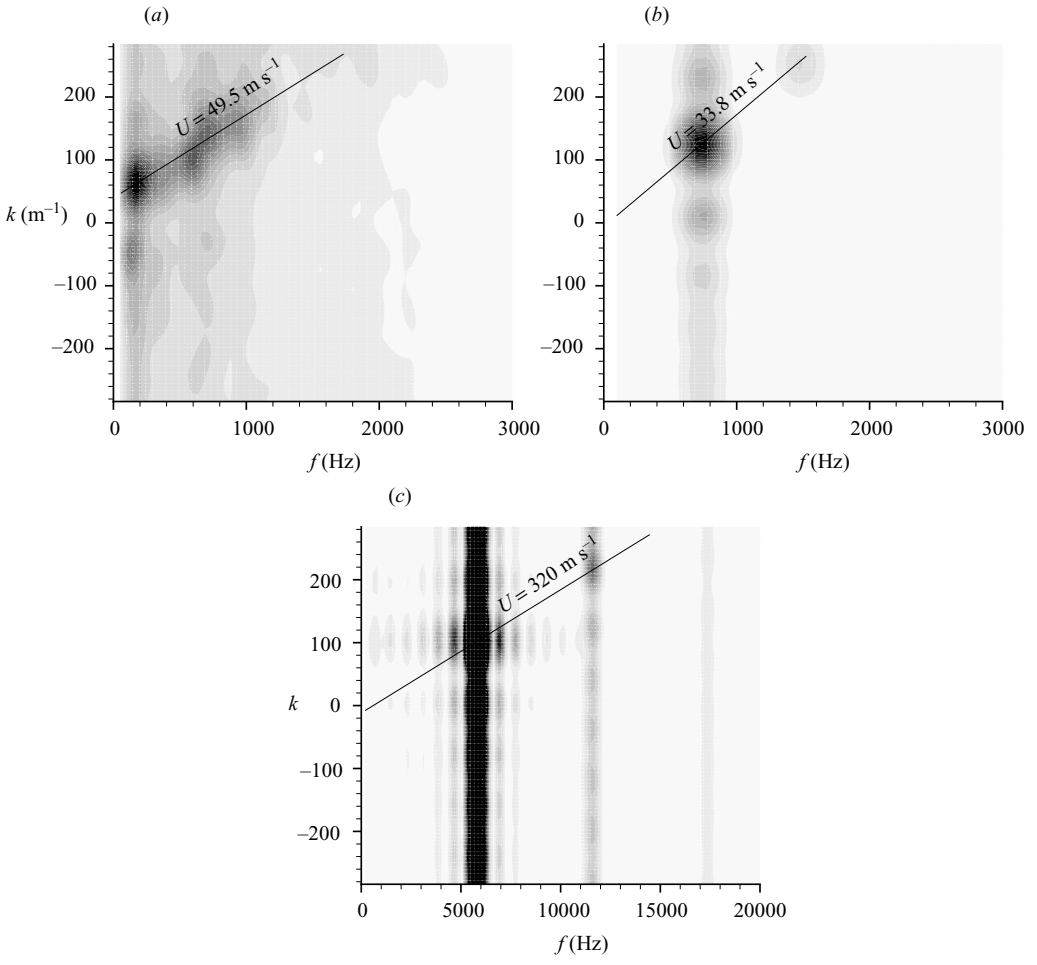


FIGURE 28. Frequency–wavenumber pressure spectra estimator $\Psi(f, k)$ (*a*) Uncontrolled case, (*b*) LF case, (*c*) HF case.

to the energy input of the forcing, the level of the entire spectra of the two controlled cases is higher than that of the uncontrolled case for the sensor C1. For the sensors C3, C5 and C10, the effect of the LF forcing is only visible on the large-scale range for $f \leqslant 6000$ Hz, unlike the HF forcing which energizes all the spectrum. As observed by Stanek *et al.* (2002*a*, *b*) and Wiltse & Glezer (1998), the effect of the HF forcing on the spectra at sensors C3, C5 and C10 is a decrease of the large-scale energy level and an increase of the small scales. Stanek *et al.* have proposed splitting the energy spectrum into two parts. The left portion of the spectrum (frequencies lower than the forcing one) has a decelerated cascade with a lower energy transfer from the large to the small scales. Since the turbulent kinetic energy production (figure 27) is lower than in the baseline case, this energy transfer is also lower. The right portion of the spectrum can have either a lower or higher energy content because of two competing influences: the lower energy transfer from the larger-scale part and the energy input of the forcing.

In summary, in the LF case, the Q-criterion isosurface has demonstrated the formation of large spanwise vortices which are convected downstream at an average velocity of $0.33U_\infty$. Pressure spectra in the mixing layer have shown that the global turbulent

https://doi.org/10.1017/S0022112006003995 Published online by Cambridge University Press

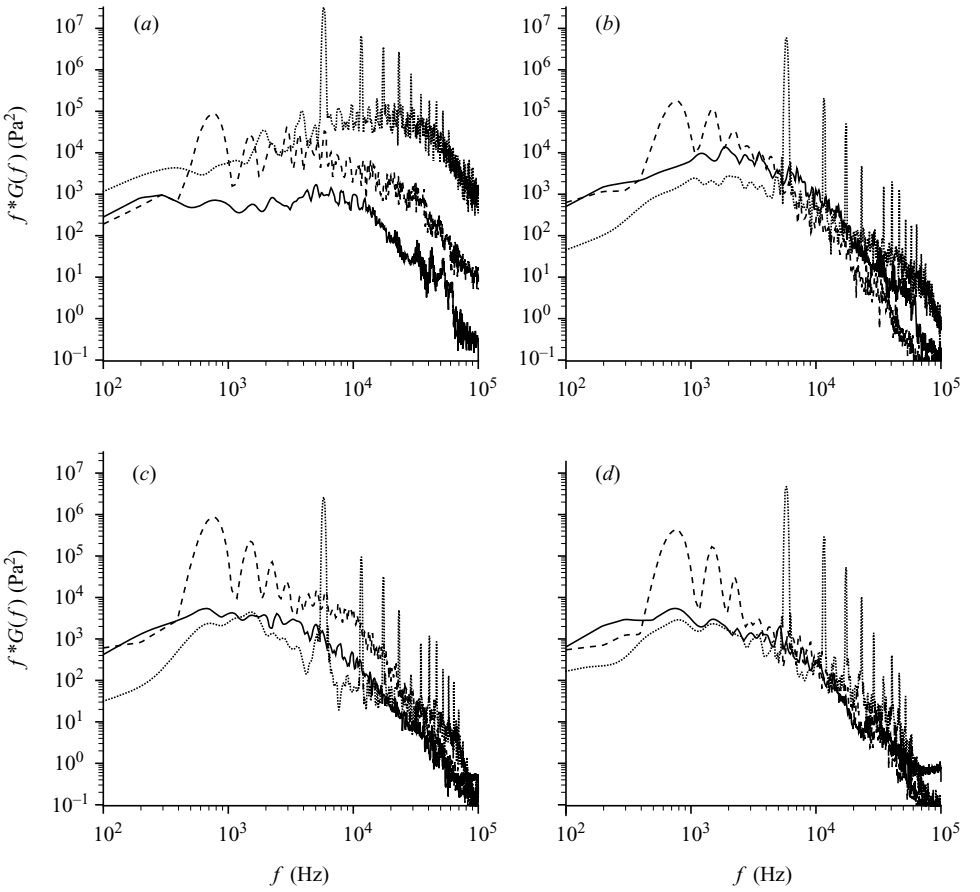


FIGURE 29. Pressure spectra along the mixing layer for four sensors (*a*: C1, *b*: C3, *c*: C5, *d*: C10) and for the three cases: uncontrolled flow (solid line), LF case (dashed line) and HF case (dotted line).

kinetic energy increase is concentrated in the large scales. The physical explanation for the 54 % separation length reduction will be established in the next section.

In the HF case, the presence of acoustic waves has been highlighted by an instantaneous pseudo-schlieren visualization. The existence of these acoustic waves has been corroborated by the increase of the streamwise velocity fluctuation level upstream of the actuator location and by an average convection velocity of 320 m s^{-1} obtained by a frequency–wavenumber analysis. The separation length increase by 43 % appears not to be due to a blockage effect induced by the synthetic jet. A decrease of the turbulent kinetic energy level and lower momentum and vorticity thicknesses have also been observed. Unlike the LF forcing case, pressure spectra in the shear layer show a reduction of the large-scale energy level. Stanek *et al.* (2002*a*, *b*) explain this reduction by a modification of the mean streamwise velocity stability properties as observed in figure 21. However, a stability analysis of the HF case is required to definitively conclude on the possible application of Stanek's model to our case.

5.4. *Low-frequency forcing case analysis*

The coherent structure location is computed using two-point two-time auto-correlation of the pressure signal. Only the uncontrolled and the LF cases are

https://doi.org/10.1017/S0022112006003995 Published online by Cambridge University Press

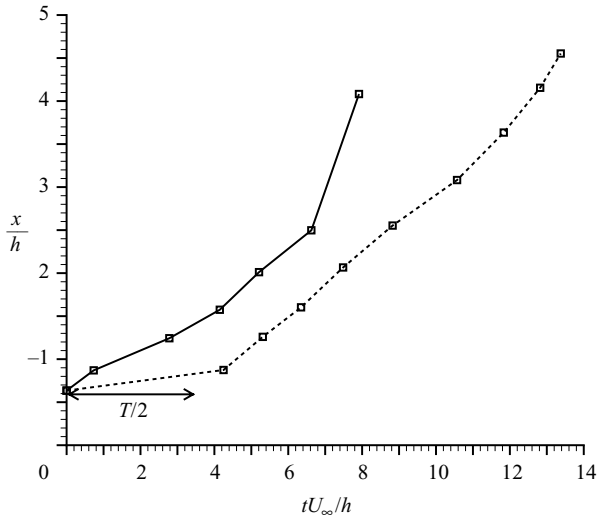


FIGURE 30. Evolution of vortex location with time estimated using two-point two-time auto-correlation of p for the unforced case (solid line) and the LF case (dashed line).

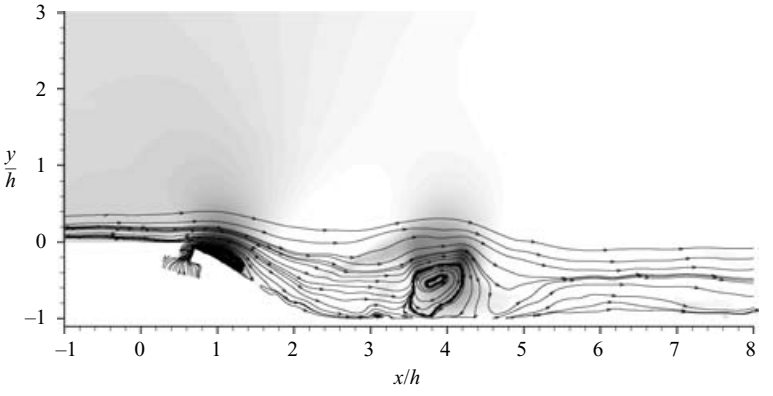


FIGURE 31. Instantaneous pressure field and streamlines showing the reattached flow between two consecutive eddies created by the low-frequency forcing.

considered here, since this kind of analysis is not useful in the HF forcing case. In the uncontrolled case, the K-H vortex location increases linearly with time between $x/h = 0.5$ and 2.5 (see figure 30). This demonstrates that the convection velocity is almost constant. In the LF case, the vortices do not move between times $tU_\infty/h = 0$ and 3.5. This corresponds to one half of the actuation period for $F^+ = 0.5$. So, during the blowing phase of the actuation, the two-dimensional vortex forms, grows in size and its circulation increases. The streamlines roll up (see figure 31). Then, during the suction phase of the actuation, the vortex leaves the orifice and is convected with a constant velocity for $tU_\infty/h = 4$. Since the flow is reattached between two consecutive vortices (figure 31) and the vortex formed just downstream of the orifice is quasi-steady during a significant part of the forcing period, high-momentum fluid is carried from the free stream toward the wall by an entrainment effect. This mechanism explains the separation length reduction.

https://doi.org/10.1017/S0022112006003995 Published online by Cambridge University Press

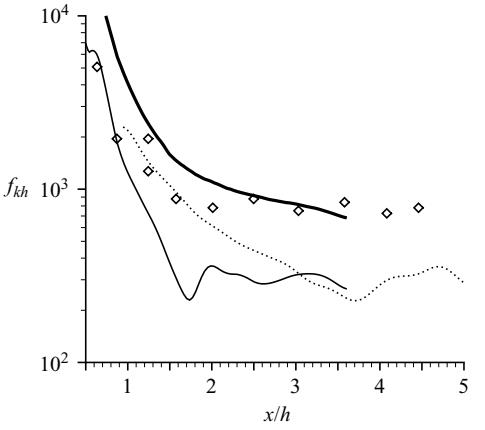


FIGURE 32. Streamwise evolution of the computed natural frequency f_{kh} as a function of position x/h (thick solid line: most amplified frequency of two-dimensional linear stability analysis (equation (5.9)), thin solid line: uncontrolled flow, dotted line: HF case, and diamond symbol: frequencies corresponding to the spectra peaks of figure 11).

5.5. *High-frequency forcing case analysis: inviscid linear stability analysis*

The basic equation for linear inviscid stability analysis of parallel shear flows is the incompressible Rayleigh equation:

$$(U - \beta/\alpha)\,[\phi'' - \alpha^2\phi] - U''\phi = 0 \tag{5.7}$$

where U is mean streamwise velocity, U'' is its second derivative in the y-direction, β is the real angular velocity, $\alpha = \alpha_r + \mathrm{i}\alpha_i$ with α_r the wavenumber and α_i the spatial growth rate, and ϕ is the complex eigenfunction which is the amplitude of the stream function. The boundary conditions for this equation are

$$\phi(-\infty) = \phi(+\infty) = 0. \tag{5.8}$$

The numerical method is the same as in Robinet, Dussauge & Casalis (2001). It relies on a spectral collocation method based on Chebyshev polynomials which provides an accurate solution of the eigenvalue problem. A standard subroutine from the LAPACK library is used to compute the eigenvalues.

The natural frequency predicted by the stability analysis is plotted as function of x/h in figure 32 for both cases. The Kelvin–Helmholtz vortex passage frequency can be also estimated by means of the local most amplified frequency of a linear stability analysis in a the case of a two-dimensional free shear layer as estimated by Huerre & Rossi (1998):

$$f_{KH}(x) \simeq 0.135\frac{\overline{U}(x)}{\delta_\omega(x)}. \tag{5.9}$$

These frequencies are decreasing functions of x/h. In the uncontrolled case, the natural frequency decreases between the separation point, which is located at $x/h = 0.5$, and $x/h = 2$. Then, the frequency is nearly constant at around 320 Hz whereas the shedding frequency observed in figure 11 is nearly 800 Hz. Because the K-H vortices are rather two-dimensional in the initial development of the mixing layer, (5.9) is expected to yield a reliable estimation of the vortex passage frequency. The natural shear layer frequency for the uncontrolled case is lower than the frequency given by (5.9). The results given by the linear stability analysis are in good agreement with the

https://doi.org/10.1017/S0022112006003995 Published online by Cambridge University Press

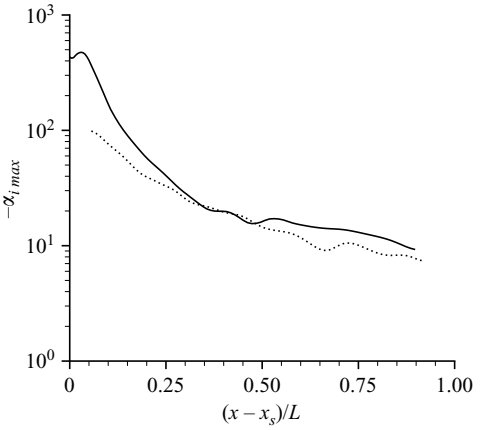


FIGURE 33. Maximum spatial growth rate as a function of position x/h (solid line: uncontrolled flow, dotted line: HF case).

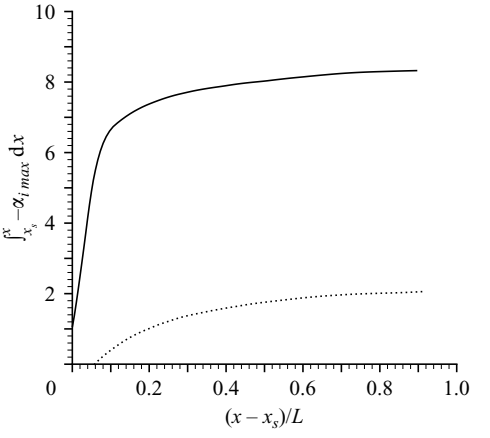


FIGURE 34. Computed amplitude $\int_{x_s}^{x} \alpha_i \,\mathrm{d}x$ as a function of position x/h (solid line: uncontrolled flow, dotted line: HF case).

frequencies associated with the spectra peaks in figure 11 for the first two points, i.e. in the region of initial development of the shear layer when the linear hypothesis is valid. Further downstream, for $x/h \geqslant 2.5$, the frequencies detected in figure 11 are in better agreement with those given by (5.9). In the HF case, the natural frequency is higher than in the uncontrolled case. It decreases continuously between $x/h = 1$ and 3.7 and then it is nearly constant around at 300 Hz.

The evolution of the maximum spatial growth rate as function of position x/h is displayed in figure 33. In the uncontrolled case, the growth rate increases from the beginning of the shear layer up to $(x - x_s)/L = 0.03$, and then it decreases continuously. In the HF case, the growth rate is always higher than in the uncontrolled case because of the higher backflow velocity. Nonetheless, the amplitude of the perturbation is not given by the local growth rate but rather by the growth rate integral from the separation point to the abscissa considered, as seen in figure 34. This figure shows that the amplitude of the perturbation in the HF case is seven times lower than in the uncontrolled case at location $(x - x_s)/L = 0.2$ and four times lower at $(x - x_s)/L = 0.9$.

https://doi.org/10.1017/S0022112006003995 Published online by Cambridge University Press

As expected from figure 33, the main part of the difference between the two levels of perturbation is observable from the separation point. Consequently, the separation length appears to be closely tied to the growth rate of the perturbations at this point. This analysis is based on the fact that a lower level of perturbation results in a reduced entrainment of momentum leading to a reduced spreading of the separated mixing layer and subsequently to an increased separation length. We find here a confirmation of Stanek's hypothesis (Stanek *et al.* (2002*a*, *b*) that the effect of the high-frequency forcing is a modification of the mean streamwise velocity field which leads to a lower perturbation amplitude.

6. Conclusion

Numerical simulations of the controlled flow over a smooth ramp have been performed to study the influence of synthetic jet frequency on the flow and to assess the efficiency of synthetic jets in reducing separation length. In the first part, LES of the separated flow has been validated through comparisons with DNS results. The agreement is very good for both the mean and fluctuating velocity profiles. Then, two different reduced frequencies with opposite effects on the separation length have been considered: a low-frequency forcing at $F^+ = 0.5$ and a high-frequency forcing at $F^+ = 4$. The first case corresponds to a vorticity-dominated mode and the second to an acoustic-dominated mode.

For $F^+ = 0.5$, the separation length is reduced by half for a velocity ratio of 0.5. This frequency corresponds to the presence of a single large vortex in the separated zone and is close to the natural shedding frequency. The LF forcing increases the turbulent kinetic energy level. Moreover, the level of turbulent kinetic energy production is twice that in the uncontrolled case and three times higher than in the HF case. A careful examination of pressure spectra in the mixing layer reveals that the increase of the energy level is restricted to the large scales. Since the flow is reattached between two consecutive vortices and the vortex formed just downstream of the orifice is quasi-steady during a significant part of the forcing period, high-momentum fluid is carried from the free stream toward the wall by an entrainment effect. This mechanism explains the separation length reduction. Afterwards, during the suction phase, this vortex leaves the orifice and is convected at an average velocity equal to $0.33U_\infty$.

The effect of the HF forcing at $F^+ = 4$ is an increase of the separation length by 43 %. Flow visualization, time-averaged streamwise velocity fluctuation profiles and two-point two-time correlations have shown that for high forcing frequency the synthetic jet generates large-amplitude sound waves and operates in an acoustic-dominated mode. Nevertheless, the forcing has a significant influence on the mean streamwise velocity profile. A linear inviscid stability analysis has demonstrated that the reason for the increase of the separation length is a lower amplitude of the perturbations than in the uncontrolled case. This is due to a lower spatial growth rate near the separation point. Consequently, the effect of the HF forcing is a modification of the mean streamwise velocity profile stability as suggested by Stanek *et al.* (2002*a*, *b*). Consistently with findings of these authors, the HF forcing decreases the turbulent kinetic energy for $x/h \geqslant 1$. This reduction is concentrated in the large scales. To our knowledge, this paper constitutes the first demonstration, by numerical simulations of a fully turbulent flow, of Stanek's hypothesis.

The authors warmly acknowledge Dr Jean-Christophe Robinet for providing the linear inviscid stability solver.

https://doi.org/10.1017/S0022112006003995 Published online by Cambridge University Press

REFERENCES

Adams, E. W. & Johnston, J. P. 1988*a* Effects of the separating shear layer on the reattachment flow structure Part 1: Pressure and turbulence quantities. *Exps. Fluids* **6**, 417–426.

Adams, E. W. & Johnston, J. P. 1988*b* Effects of the separating shear layer on the reattachment flow structure Part 2: Reattachment length and wall shear stress. *Exps. Fluids* **6**, 493–499.

Amitay, M. & Glezer, A. 2002 Role of actuation frequency in controlled flow reattachment over stalled airfoil. *AIAA J.* **40** (2) 203–216.

Bhattacharjee, S., Scheelke, B. & Troutt, T. R. 1986 Modification of vortex interactions in a reattaching separated flow. *AIAA J.* **24**, 623–629.

Browand, F. K. & Troutt, T. R. 1985 The turbulent mixing layer: geometry of large vortices. *J. Fluid Mech.* **158**, 489–509.

Brown, G. L. & Roshko, A. 1974 On density effects and large structure in turbulent mixing layers. *J. Fluid Mech.* **64**, 775–816.

Brunn, A. & Nitsche, W. 2003 Separation control by periodic excitation in a turbulent axisymmetric diffuser flow. *J. Turb.* **4** (9) 1–13.

Castro, I. P. & Haque, A. 1987 The structure of a turbulent shear layer bounding a separation region. *J. Fluid Mech.* **179**, 439–468.

Chandrsuda, C. & Bradshaw, P. 1981 Turbulence structure of a reattaching mixing layer. *J. Fluid Mech.* **110**, 171–194.

Chen, Y., Liang, S., Aung, K., Glezer, A. & Lagoda, J. 1999 Enhanced mixing in a simulated combustor using synthetic jet actuators. *AIAA Paper* 99-0449.

Cherry, N. J., Hillier, R. & Latour, M. E. M. P. 1984 Unsteady measurements in a separated and reattaching flow. *J. Fluid Mech.* **144**, 13–46.

Chun, K. B. & Sung, H. J. 1996 Control of turbulent separated flow over a backward-facing step by local forcing. *Exps. Fluids* **21**, 417–426.

Chun, K. B. & Sung, H. J. 1998 Visualization of a locally-forced separated flow over a backward-facing step. *Exps. Fluids* **25**, 133–142.

Dacles-Mariani, J., Zilliac, G. G., Chow, J. S. & Bradshaw, P. 1995 Numerical/Experimental study of a wingtip vortex in the near field. *AIAA J.* **33**, 1561–1568.

Dandois, J., Garnier, E. & Sagaut, P. 2006 Unsteady Simulation of Synthetic Jet in a Crossflow. *AIAA J.* **44**, 225–238.

Darabi, A. & Wygnanski, I. 2004*a* Active management of naturally separated flow. Part 1. The forced reattachment process. *J. Fluid Mech.* **510**, 105–129.

Darabi, A. & Wygnanski, I. 2004*b* Active management of naturally separated flow. Part 2. The separation process. *J. Fluid Mech.* **510**, 131–144.

Deck, S. 2005*a* Numerical simulation of transonic buffet over a supercritical airfoil. *AIAA J.* **43**, 1556–1566.

Deck, S. 2005*b* Zonal detached-eddy simulation of the flow around a high-lift configuration. *AIAA J.* **43**, 2372–2384.

Dejoan, A. & Leschziner, M. A. 2004 Large eddy simulation of periodically perturbed separated flow over a backward-facing step. *Intl J. Heat Fluid Flow* **25**, 581–592.

Devenport, W. J. & Sutton, E. P. 1991 Near-wall behavior of separated and reattaching flow. *AIAA J.* **29**, 25–31.

Driver, D. M., Seegmiller, H. L. & Marvin, J. 1983 Unsteady behavior of a reattaching shear layer. *AIAA Paper* 83-1712.

Eaton, J. K. & Johnston, J. P. 1980 Turbulent flow reattachment: an experimental study of the flow and structure behind a backward-facing step. *Tech. Rep.* MD 39. Department of Mechanical Engineering, Stanford University.

Eaton, J. K. & Johnston, J. P. 1981 A review of research on subsonic turbulent flow reattachment . *AIAA J.* **19**, 1093–1100.

Edwards, J. R. & Liou, M. S. 1998 Low-diffusion flux-splitting methods for flows at all speeds. *AIAA J.* **36**, 1610–1617.

Friedrich, R. & Arnal, M. 1990 Analysing turbulent backward-facing step flow with the lowpass-filtered Navier-Stokes equations. *J. Wind Engng Ind. Aerodyn.* **35**, 101–128.

Glezer, A., Amitay, M. & Honohan, A. M. 2005 Aspects of low- and high-frequency aerodynamic flow control. *AIAA J.* **43**, 1501–1511.

https://doi.org/10.1017/S0022112006003995 Published online by Cambridge University Press

Hasan, M. A. 1992 The flow over a backward-facing step under controlled perturbation: laminar separation. *J. Fluid Mech.* **238**, 73–96.

Heenan, A. F. & Morrison, J. F. 1998 Passive control of pressure fluctuations generated by separated flows. *AIAA J.* **36**, 1014–1022.

Ho, C.-M. & Huang, L.-S. 2002 Subharmonics and vortex merging in mixing layer. *J. Fluid Mech.* **119**, 443–473.

Holman, R., Utturkar, Y., Mittal, R., Smith, B. L. & Cattafesta, L. 2005 Formation criterion for synthetic jets. *AIAA J.* **43**, 2110–2116.

Huang, H. T. & Fiedler, H. E. 1997 A DPIV study of a starting flow downstream of a backward-facing step. *Exps. Fluids* **23**, 395–404.

Hudy, L. M., Naguib, A. M. & Humphreys, W. M. 2003 Wall-pressure-array measurements beneath a separating/reattaching flow region. *Phys. Fluids* **15**, 706–717.

Huerre, P. & Rossi, M. 1998 Hydrodynamic instabilities in open flows. In *Hydrodynamics and Nonlinear Instabilities* (ed. C. Godrèche & P. Manneville). Cambridge University Press.

Ingard, U. 1953 On the theory and design of acoustic resonators. *J. Acoust. Soc. Am.* **25** (6) 1037–1061.

Jovic, S. 1996 An experimental study of a separated/reattached flow behind a backward-facing step. $Re_H = 37,000$. *NASA Tech. Mem.* 110384.

Kiya, M. & Sasaki, K. 1985 Structure of large-scale vortices and unsteady reverse flow in the reattaching zone of a turbulent separation bubble. *J. Fluid Mech.* **154**, 463–491.

Kiya, M., Shimizu, M. & Mochizuki, O. 1997 Sinusoidal forcing of a turbulent separation bubble. *J. Fluid Mech.* **342**, 119–139.

Larchevêque, L., Sagaut, P., Lê, T. H. & Comte, P. 2004 Large-eddy simulation of a compressible flow in a three-dimensional open cavity at high reynolds number. *J. Fluid Mech.* **516**, 265–301.

Larchevêque, L., Sagaut, P., Mary, I. & Labbé, O. 2003 Large-eddy simulation of a compressible flow past a deep cavity. *Phys. Fluids* **15**, 193–210.

Le, H., Moin, P. & Kim, J. 1997 Direct numerical simulation of turbulent flow over a backward-facing step. *J. Fluid Mech.* **330**, 349–374.

Lee, I. & Sung, H. J. 2001 Characteristics of wall pressure fluctuations in separated and reattaching flows over a backward-facing step: Part I. Time-mean statistics and cross-spectral analyses. *Exps. Fluids* **30**, 262–272.

Lee, I. & Sung, H. J. 2002 Multiple-arrayed pressure measurement for investigation of the unsteady flow structure of a reattaching shear layer. *J. Fluid Mech.* **463**, 377–402.

Liu, Y. Z., Kang, W. & Sung, H. J. 2005 Assessment of the organization of a turbulent separated and reattaching flow by measuring wall pressure fluctuations. *Exps. Fluids* **38**, 485–493.

Lund, T. S., Wu, X. & Squires, K. D. 1998 Generation of turbulent inflow data for spatially developing turbulent boundary layer simulations. *J. Comput. Phys.* **140**, 233–258.

Mabey, D. G. 1972 Analysis and correlation of data on pressure fluctuations in separated flows. *J. Aircraft* **9**, 642–645.

Mary, I. & Sagaut, P. 2002 LES of a flow around an airfoil near stall. *AIAA J.* **40**, 1139–1145.

Morris, S. C. & Foss, J. F. 2003 Turbulent boundary layer to single-stream shear layer: the transition region. *J. Fluid Mech.* **494**, 187–221.

Na, Y. & Moin, P. 1998 The structure of wall-pressure fluctuations in turbulent boundary layers with adverse pressure gradient and separation. *J. Fluid Mech.* **77**, 347–373.

Naguib, A. M. & Hudy, L. M. 2003 Stationary and propagating low-frequency wall-pressure disturbances in a separating/reattaching flow. *AIAA Paper* 2003-1126.

Narayanan, S. & Banaszuk, A. 2003 Experimental study of a novel active separation control approach. *AIAA Paper* 2003-60.

Neto, A. S., Grand, D., Metais, O. & Lesieur, M. 1993 A numerical investigation of the coherent vortices in turbulence behind a backward-facing step. *J. Fluid Mech.* **256**, 1–25.

Neumann, J. & Wengle, H. 2004*a* Coherent structures in controlled separated flow over sharp-edged and rounded steps. *J. Turb.* **5** (22) 1–24.

Neumann, J. & Wengle, H. 2004*b* LES of controlled turbulent flow over a rounded step. In *Direct and Large Eddy Simulation V* (ed. R. Friedrich *et al.*), pp. 557–564. Kluwer.

Oster, D. & Wygnanski, I. 1982 The forced mixing layer between parallel streams. *J. Fluid Mech.* **123**, 91–130.

https://doi.org/10.1017/S0022112006003995 Published online by Cambridge University Press

Péchier, M., Guillen, P. & Gayzac, R. 2001 Magnus effect over finned projectiles. *J. Spacecrafts Rockets* **38**, 542–549.

Robinet, J.-C., Dussauge, J.-P. & Casalis, G. 2001 Wall effect on the convective-absolute boundary for the compressible shear layer. *Theoret. Comput. Fluid Dyn.* **15**, 143–163.

Ruderich, R. & Fernholz, H. H. 1986 An experimental investigation of a turbulent shear flow with separation, reverse flow and reattachment. *J. Fluid Mech.* **163**, 283–322.

Rusak, Z. & Eisele, I. R. 2005 Controlled manipulation of small- and large- scales in a turbulent shear layer, Part II: Stability studies. *AIAA Paper* 2005-4754.

Sagaut, P. 2002 *Large-Eddy Simulation for Incompressible Flows, An Introduction*, 2nd edn. Springer.

Sagaut, P., Garnier, E., Tromeur, E., Larchevêque, L. & Labourasse, E. 2004 Turbulent inflow conditions for les of compressible wall bounded flows. *AIAA J.* **42**, 469–477.

Scarano, F., Benocci, C. & Riethmuller, M. L. 1999 Pattern recognition analysis of the turbulent flow past a backward facing step. *Phys. Fluids* **11**, 3808–3818.

Seifert, A., Bachart, T., Koss, D., Shepshelovich, M. & Wygnanski, I. 1993 Oscillatory blowing: a tool to delay boundary layer separation. *AIAA J.* **31**, 2052–2060.

Seifert, A. & Pack, L. G. 2002 Active flow separation control on wall-mounted hump at high Reynolds numbers. *AIAA J.* **40**, 1363–1372.

Shuster, J. M., Pink, R. J., McEligot, D. M. & Smith, D. R. 2005 The interaction of a circular synthetic jet with a cross-flow boundary layer. *AIAA Paper* 2005-4749.

Sigurdson, L. W. 1995 The structure and control of a turbulent reattaching flow. *J. Fluid Mech.* **298**, 139–165.

Simpson, R. L. 1989 Turbulent boundary-layer separation. *Annu. Rev. Fluid Mech.* **21**, 205–234.

Smith, B. L. & Glezer, A. 2002 Jet vectoring using synthetic jets. *J. Fluid Mech.* **458**, 1–34.

Spalart, P. R. 1988 Direct simulation of a turbulent boundary layer. *J. Fluid Mech.* **187**, 61–98.

Spazzini, P. G., Iuso, G., Onorato, M., Zurlo, N. & Cicca, G. M. D. 2001 Unsteady behavior of back-facing step flow. *Exps. Fluids* **30**, 551–561.

Stanek, M. J., Raman, G., Kibens, V., Ross, J. A., Odedra, J. & Peto, J. W. 2000 Control of cavity resonance through very high frequency forcing. *AIAA Paper* 2000-1905.

Stanek, M. J., Raman, G., Ross, J. A., Odedra, J., Peto, J., Alvi, F. & Kibens, V. 2002*a* High frequency acoustic suppression – The role of mass flow, the notion of superposition and the role of inviscid instability – A new model (Part II). *AIAA Paper* 2002-2404.

Stanek, M. J., Sinha, N., Seiner, J. M., Pearce, B. & Jones, M. I. 2002*b* High frequency flow control – Suppression of aero-optics in tactical directed energy beam propagation & The birth of a new model (Part I). *AIAA Paper* 2002-2272.

Tihon, J., Legrand, J. & Legentilhomme, P. 2001 Near-wall investigation of backward-facing step flows. *Exps. Fluids* **31**, 484–493.

Troutt, T. R., Sheelke, B. & Norman, T. R. 1984 Organized structures in a reattaching separated flow field. *J. Fluid Mech.* **143**, 413–427.

Vreman, A. W. 1995 Direct and large eddy simulation of the compressible turbulent mixing layer. PhD thesis, University of Twente, Twente.

Vukasinovic, B., Lucas, D. G. & Glezer, A. 2005 Controlled manipulation of small- and large-scales in a turbulent shear layer, Part I: Experimental studies. *AIAA Paper* 2005-4753.

Wengle, H., Huppertz, A., Bärwolff, G. & Janke, G. 2001 The manipulated transitional backward-facing step flow: an experimental and direct numerical simulation investigation. *Eur. J. Mech. B Fluids* **20**, 25–46.

Wiltse, J. M. & Glezer, A. 1998 Direct excitation of small-scale motions in free shear flows. *Phys. Fluids* **20**, 25–46.

Yang, Z. & Voke, P. R. 2001 Large-eddy simulation of boundary-layer separation and transition at a change of surface curvature. *J. Fluid Mech.* **439**, 305–333.

Yoshioka, S., Obi, S. & Masuda, S. 2001*a* Organized vortex motion in periodically perturbed turbulent separated flow over a backward-facing step. *Intl J. Heat Fluid Flow* **22**, 301–307.

Yoshioka, S., Obi, S. & Masuda, S. 2001*b* Turbulence statistics of periodically perturbed flow over backward facing step. *Intl J. Heat Fluid Flow* **22**, 393–401.

https://doi.org/10.1017/S0022112006003995 Published online by Cambridge University Press